Clarification of Mechanisms of Protonic Photovoltaic Action Initiated by Photoexcitation of Strong Photoacids Covalently Bound to Hydrated Nafion Cation-Exchange Membranes Wetted by Aqueous Electrolytes

Journal:	*Energy & Environmental Science*
Manuscript ID	EE-ART-02-2021-000482.R2
Article Type:	Paper
Date Submitted by the Author:	11-Jul-2021
Complete List of Authors:	Luo, Simon; University of California, Chemistry White, William; University of California, Chemistry Cardon, Joseph; Brigham Young University, Chemistry and Biochemistry Ardo, Shane; University of California, Chemistry

SCHOLARONE™
Manuscripts

Broader Context (200 words max)

Development of functional materials for light-to-ionic power conversion may lead to new technologies for desalination, dialysis, and separations. Coupling of light to ion transport is of specific interest because the potential needed to drive these ionic processes is small in comparison to that generated by commercial solar cells, i.e. >0.5 V. For example, the minimum potential required to concentrate salt by two orders-of-magnitude, which represents the difference in salt between high-salinity ocean water and low-salinity potable water, is <0.25 V at room temperature. Such a small required photovoltage suggests that less-efficient photoconverters can be used, which supports the development of lightweight and flexible devices based on organic materials. Herein we demonstrate that polymeric cation-exchange membranes covalently modified with photoacid dye molecules and wetted by single-salt-containing aqueous electrolytes are able to transduce visible light into protonic power. This integrated design and power-conversion process circumvents the formation of intermediate electronic species, enabling a more direct use of the energy in light. While observed photovoltages are small, we show that performance is limited by unoptimized molecular photoacid dye sensitizers that photogenerate little-to-no minority-carrier hydroxides. New knowledge gained from our efforts will aid in the development of devices for efficient light-to-ionic power conversion.

Clarification of Mechanisms of Protonic Photovoltaic Action Initiated by Photoexcitation of Strong Photoacids Covalently Bound to Hydrated Nafion Cation-Exchange Membranes Wetted by Aqueous Electrolytes

Simon Luo,[1] William White,[1] Joseph M. Cardon,[1] and Shane Ardo[1,2,3*]

[1]Department of Chemistry, University of California Irvine, Irvine, CA 92617 USA

[2]Department of Materials Science & Engineering, University of California Irvine, Irvine, CA 92617 USA

[3]Department of Chemical & Biomolecular Engineering, University of California Irvine, Irvine, CA 92617 USA

* ardo@uci.edu

Abstract

Junctions that form at interfaces of electronic semiconductors can lead to space–charge depletion regions that result in diode behavior through current rectification. Space–charge regions are not unique to semiconductor interfaces and also form at and across ion-exchange membranes, with properties that can be tuned by varying the concentration of ions in contacting phase(s). Using this as a guide, and motivated by traditional dye-sensitized solar cells, we bathed photoacid-dye-sensitized cation-exchange membranes in aqueous solutions of varied electrolyte concentration and analyzed them for their ability to exhibit photovoltaic action. As predicted by Donnan membrane theory and semiconductor theory, the thermodynamic properties of each contacting phase determined the magnitude and sign of the net built-in electric potential difference. Open-circuit photovoltages were directly related to these electric potential differences, albeit the sign of photovoltages was opposite ("reverse") of that expected based on the sign of net electric potential differences across the membrane. Mechanistic details gleaned using nanosecond transient absorption spectroscopy indicate that state-of-the-art photoacids only photogenerate protons as the mobile charged species. Because our dye-sensitized cation-exchange membranes were infiltrated with protons, this means that minority-carrier hydroxides were not able to elicit photovoltaic action by standard minority-carrier-dominated charge separation. Instead, our data is consistent with charge separation of a proton from its photoacid conjugate base that is driven by intrinsic liquid-junction-forming crossover of acid to result in bulk membrane polarization and "reverse" photovoltaic action. Conclusions from our data suggest design guidelines for future efforts to use water as a protonic semiconductor for light-to-ionic power conversion.

Introduction

Conversion of light into electricity through photogeneration of mobile charged species[1–3] is termed photovoltaic action. This process is efficient when species of one charge type are collected at a contact more rapidly, and thus more selectively, than species of the other charge type, which is a hallmark of current rectification.[4,5] Current rectification and sunlight absorption are important factors for effective photovoltaic action. Nearly all examples of photovoltaic action have used electronic semiconductors, because of their demonstrated ability to be fabricated into diodes that effectively rectify current.[6] Semiconductors that are ineffective visible-light absorbers use dye molecules to sensitize them to absorption of more solar photons.[7] Many examples of these dye-sensitized solar energy conversion devices exist.[8–10] The most common have dyes positioned at an interface between an inorganic semiconductor and a redox-active liquid electrolyte,[9] or incorporated into a polymeric material and rely on exciton diffusion to reach interfaces and charge separate, such as in organic photovoltaics.[11,12]

Recently, our group reported an alternative dye-sensitized construct for conversion of visible light into useful power that did not rely on electronic mobile charged species or an interface for initial charge separation.[13–15] These composite materials consisted of a perfluorosulfonic acid (PFSA) ion-exchange membrane, like Nafion, with covalently bound derivatives of pyrenol-based reversible photoacid molecules, 8-hydroxypyrene-1,3,6-trisulfonylethylenediammonium (HPTSA), as dye sensitizers. *Unique to our efforts is that we used water as the protonic semiconducting medium.* Doping of the water semiconductor was achieved by infiltrating it into hydrophilic domains of the dopant-containing PFSA polymeric scaffold. Through its covalent modification, this scaffold prevented macroscopic transport of dopant functional groups and photoacid molecular dyes, while enabling generation of mobile H^+ and/or OH^- in the water

semiconductor, predominantly due to thermal excitation of dopants and photochemical excitation of dyes. Absorption of visible light by the photoacid resulted in a shift in its electron density thereby weakening a protic bond, which increased the thermodynamic favorability for deprotonation.[16] Kinetically, excited-state proton transfer was able to occur only when the excited-state lifetime was longer than the time it took to transfer a proton directly to solvent to form $H^+(aq)$, or directly to $OH^-(aq)$ to form H_2O. When this occurred, subsequent return of the excited-state deprotonated photoacid back to its electronic ground state resulted in formation of the conjugate base of the photoacid, which was ultimately reprotonated by $H^+(aq)$, or by H_2O to form $OH^-(aq)$. Overall, this sensitization cycle used visible-light absorption to generate mobile protonic charged species.

To enable generation of large photovoltaic effects, an important property of many, but not all,[4,5,17] electronic semiconductors is the existence of an electrostatic space–charge depletion region that results in the property of current rectification.[4,17] Space–charge depletion regions are typically formed by diffusing dopants into a surface of an oppositely doped semiconductor to create a buried pn-junction, or by contacting the semiconductor with a metal whose work function differs significantly from that of the semiconductor, which creates a Schottky junction at the semiconductor|metal interface. Photon absorption results in net generation of mobile electron and hole charged species that are effectively separated by the space–charge depletion region and subsequently collected at selective contacts. Differences in the electrochemical potentials of electrons and holes at the contacts can be used to power electronic devices, and there is no net generation of chemical species. Analogous to the creation of a Schottky junction, one can also contact one side of an electronic semiconductor with a liquid electrolyte solution that contains redox-active molecules to form a space–charge depletion region at the semiconductor|liquid

interface.[18] Photon absorption also results in net generation of mobile electron and hole charged

species, however, uniquely these species react with redox-active molecules to ultimately generate

electronic power, and form no net chemical species, or drive net chemical redox reactions.[19,20] The

benefit of these photoelectrochemical constructs is that formation of a space–charge depletion

region is a noninvasive process because in general liquid electrolytes inherently conformally coat

even nanostructured electrode surfaces. This means that pinhole-free junctions that do not greatly

perturb the surface chemistry of the semiconductor are possible. Notable fundamental science

studies by Lewis and colleagues showed that the magnitude of the open-circuit photovoltage (V_{oc})

of a semiconductor–liquid junction scales directly with the reduction potential of the liquid

electrolyte,[21,22] which altered the interfacial barrier height, the magnitude of the built-in electric

(electrostatic) potential, and the width of the space–charge depletion region. They used a

semiconductor consisting of high-quality crystalline silicon, doped p-type or n-type and that

contained one ohmic metallurgical back contact to provide low-impedance charge collection to an

external circuit, liquid electrolyte consisting of acetonitrile or methanol containing $LiClO_4$, and a

redox couple consisting of metallocenes/metalloceniums or viologens that were all mutually

compatible and stable. Follow-on work in part overcame instability in aqueous electrolytes through

methylation of the freshly-etched Si(111) surface[23] and furthered these studies by implementing

liquid junctions at both the front and back contacts to the semiconductor.[24,25] Leveraging this

knowledgebase and expanding it to the analysis of dye-sensitized ion-exchange-membrane–liquid-

junction assemblies is the aim of the work reported herein.

It is well-known in membrane science that electrostatic space–charge regions also form

across permselective-membrane|solution and membrane|membrane interfaces.[26,27] In the presence

of various charged species, resulting *steady-state* electric potential differences are reasonably

quantified by the Henderson and Goldman equations.[28–31] When only two species of opposite sign are the dominant mobile charged species at a membrane|solution interface, such as when the solution contains only one soluble salt, these equations quantify *equilibrated* Donnan potentials. In this case, and by analogy to space–charge regions in electronic semiconductors, Donnan theory predicts that a thermally and electrochemically equilibrated electric potential difference exists across each interface.[32,33] Processes to attain thermal and electrochemical equilibration of mobile charged species across liquid junctions are the same for semiconductors and ion-exchange membranes (Figure 1). Driven by gradients in the activity, and therefore chemical potential, of mobile charged species, they diffuse across said interfaces. This results in charge
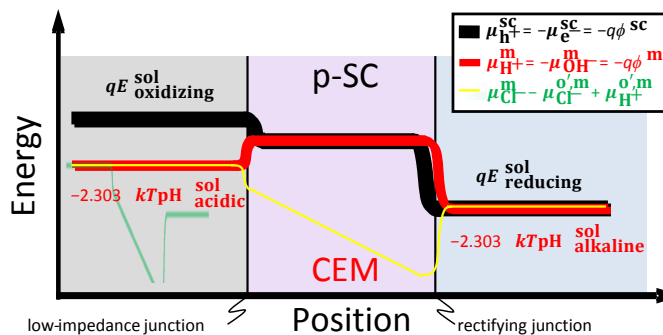

Figure 1. Energy-level diagram for a semiconductor–liquid-junction (sc) device, which is analogous to a Schottky-junction device, and consists of a p-type semiconductor (p-SC) wetted on each side by a solution that contains redox species with reduction potential, E_i^{sol}. The chemical potential of electrons, $\mu_{e^-}^{sc}$, and holes, $\mu_{h^+}^{sc}$, at each location are equal and opposite, which signifies chemical equilibrium at each location. The magnitude of $\mu_{e^-}^{sc}$ at each location is equal to the magnitude of the electric potential contribution, $q\Phi^{sc}$, meaning that each species has a spatially invariant electrochemical potential (Fermi level), which signifies electrochemical equilibrium across the entire device geometry. Also illustrated is a membrane–liquid-junction (m) device that consists of a cation-exchange membrane (CEM) wetted on each side by a solution at a fixed pH value, pH_i^{sol}, which results in analogous properties for protons, $\mu_{H^+}^{m}$, hydroxides, $\mu_{OH^-}^{m}$, and their respective electric potential contribution, $q\Phi^{m}$. Notable differences between a desired semiconductor–liquid-junction device and a membrane–liquid-junction device are that *(i)* Φ^{sc} predominantly varies in the semiconductor phase, rather than in the solution phases, while Φ^{m} predominantly varies in the solution phases, rather than in the membrane phase; *(ii)* a perfectly ohmic contact cannot form at the low-impedance charge-collection junction of the CEM because that would completely remove Donnan exclusion, which is required for the membrane to be charge selective for cations, like a p-type semiconductor; and *(iii)* ions of opposite charge to the mobile charged species, e.g. Cl⁻ counterions, necessarily infiltrate into the CEM as coions and result in non-equilibrium conditions across the entire device geometry. For ease of visualization, the chemical potential of Cl⁻, $\mu_{Cl^-}^{m}$, is referenced to the standard concentration chemical potential of H⁺, $\mu_{H^+}^{o',m}$, where "concentration" is commonly used for equilibrium constants and is analogous to "formal" for reduction potentials.

separation, and thus formation of a space–charge region, meaning that electric fields and electric potential differences exist to oppose the chemical potential difference of the mobile charged species. When these potentials are equal and opposite, the species has reached electrochemical equilibrium, meaning that the species has a spatially invariant electrochemical potential. Equilibrated electric potential differences are analogous to space–charge regions that are responsible for the current–potential behavior of both rectifying charge-separation junctions and low-impedance charge-collection junctions in electronic semiconductors. Control over these electrostatic properties are thus critical to realization of effective ionic diodes, which further motivates development of design principles for light-to-ionic power conversion using dye-sensitized ion-exchange membranes.

The interfacial (int) Donnan (D) electric potential difference between the bulk quasi-neutral region of the solution (sol) *versus* the bulk quasi-neutral region of the membrane (mem), ϕ_D^{int}, is calculated using the following equation, which is derived in the Supplementary Information in the subsection titled "Donnan Theory and the Capacity for Ion Exclusion,"

$$\phi_D^{int} = -\frac{RT}{zF}\ln\left(\frac{a^{sol}}{a^{mem}}\right) \tag{1}$$

where R is the gas constant (J mol^{-1} K^{-1}), T is temperature (K), F is the Faraday constant (C mol^{-1}), z is the charge of the majority-carrier counterion species, and a is the activity of the majority-carrier species on each side of the interface. Because a wetted ion-exchange membrane has two membrane|solution interfaces, there are two ϕ_D^{int} that contribute to the measured net Donnan membrane potential, ϕ_D^{mem}. Using **Equation 1**, and the fact that the bulk quasi-neutral region of the membrane is a common reference state, leads to the following,

$$\phi_D^{mem} = \left(\phi_D^{int,WE}\right) + \left(-\phi_D^{int,CE}\right) = \frac{RT}{zF}\ln\frac{a^{sol,CE}}{a^{sol,WE}} = \frac{(\ln 10)RT}{zF}\left(pX^{WE} - pX^{CE}\right) \qquad (2)$$

where pX stands for "$-\log a^{sol}$," WE stands for nearer to the working electrode, and CE stands for nearer to the counter electrode. The concept of a membrane reference state and the form of **Equations 1 and 2** are motivated by those commonly used to represent the Nernst reduction potential of an electrode|solution interface, E_N^{int}, and the net Nernst redox potential of an electrochemical cell, E_N^{redox}, as follows,

$$E_N^{int} = E_N^{o,int} - \frac{RT}{nF}\ln\left(\frac{\left(a_{red}^{sol}\right)^{\nu_{red}}}{\left(a_{ox}^{sol}\right)^{\nu_{ox}}}\right) = E_N^{o',int} - \frac{RT}{nF}\ln\left(\frac{\left(c_{red}^{sol}\right)^{\nu_{red}}}{\left(c_{ox}^{sol}\right)^{\nu_{ox}}}\right) \qquad (3)$$

$$E_N^{redox} = \left(E_N^{int,WE}\right) + \left(-E_N^{int,CE}\right) = \left(E_N^{o',int,WE} - E_N^{o',int,CE}\right) + \frac{RT}{nF}\ln\left(\frac{\left(c_{ox}^{WE}\right)^{\nu_{ox}^{WE}}\left(c_{red}^{CE}\right)^{\nu_{red}^{CE}}}{\left(c_{red}^{WE}\right)^{\nu_{red}^{WE}}\left(c_{ox}^{CE}\right)^{\nu_{ox}^{CE}}}\right) \qquad (4)$$

where $E_N^{o,int}$ and $E_N^{o',int}$, respectively, stand for the standard reduction potential and formal reduction potential including contributions from activity coefficients and standard-state concentrations, n is the number of electrons transferred in the redox reaction, and ν and c are the relative stoichiometric number and concentration of the reduced (red) or oxidized (ox) species, respectively, that together make up the reaction quotient, $Q = \frac{\left(c_{ox}^{WE}\right)^{\nu_{ox}^{WE}}\left(c_{red}^{CE}\right)^{\nu_{red}^{CE}}}{\left(c_{red}^{WE}\right)^{\nu_{red}^{WE}}\left(c_{ox}^{CE}\right)^{\nu_{ox}^{CE}}}.$

In our previous studies,[13,15] electric potential differences across membranes were small and unstable due to the presence of transient processes such as crossover of ionic mobile charged species that resulted in partial neutralization of space–charge regions. This occurred because large concentrations of different salt cations, i.e. H^+(aq) from 1 M H_2SO_4(aq) and Na^+(aq) from 1 M NaOH(aq), were present in the aqueous electrolytes that wetted each side of the cation-exchange membrane. This meant that one side of the membrane contained a large concentration of H^+ that

diffused to the alkaline side, while the other side of the membrane contained a large concentration of Na^+ that diffused to the acidic side. Because these coupled processes resulted in a charge-neutral exchange of ions, their transport occurred quickly, thus significantly influencing electric potential differences at each membrane|solution interface and rapidly progressing the system to overall equilibrium, where no gradient in electrolyte would exist. Herein we overcame these limitations by incorporating several key advances to our experimental protocols and molecularly modified materials in order to significantly improve data resolution and advance our understanding of mechanistic details of photovoltaic action from photoacid-sensitized ion-exchange membrane constructs. These included use of only one mobile cation in all experiments, i.e. H^+, by wetting the cation-exchange membrane with various concentrations of aqueous acidic electrolyte only, i.e. HCl(aq); and subsequently, use of Ag/AgCl wires immersed directly into the HCl(aq) electrolytes as potential-sensing electrodes to prevent salt from leaking into the electrochemical cell, which occurs using typical fritted reference electrodes; and use of larger concentrations of photoacids in our membranes, which resulted in decreased concentrations of fixed-charge groups, due to covalent bonding of the photoacids to dopant sulfonate species, and therefore properties more similar to a doped semiconductor than a metal. This enabled us to, for the first time, controllably and reproducibly vary the properties of *stable* dye-sensitized and semiconducting-water-infiltrated PFSA-based membrane and its two contacting aqueous phases, each at a specific pH value, to generate a range of built-in Donnan electric potential differences across each membrane|solution interface. By analogy to the prior work of Lewis, Grimm, and colleagues using silicon–liquid-electrolyte contacts,[21,22] instead of the solution containing a soluble redox couple of varying reduction potential, we used an analogous aqueous electrolyte and varied its pH; instead of doped crystalline silicon, we used a water-infiltrated doped ion-exchange membrane. We also used

nanosecond transient absorption spectroscopy to interrogate critical mechanisms and timescales of processes that occur during the sensitization cycle for photoacid dye sensitizers. Using these protocols, polymeric materials scaffolds, and new knowledge of the photoacid dye sensitization cycle, we furthered the fundamental understanding for how light and water can be used to photogenerate ionic currents, which may be of use for application in direct light-driven desalination.[14,34,35]

Experimental

Reagents and Chemicals. The following reagents were used as received from the indicated suppliers: hydrochloric acid (36.5-38.0%, Fisher Chemical), perchloric acid (70%, Alfa Aesar), sodium chloride (>99%, Fischer Chemical), sodium hydroxide (>95%, Macron Fine Chemicals), Nafion NR-212 poly(perfluorosulfonic acid) membrane (2 mil (50.8 μm) thick, equivalent weight (EW) = 1100, Ion Power), Nafion precursor poly(perfluorosulfonyl fluoride) membrane (2 mil (50.8 μm) thick, EW = 1100, C.G. Processing), carbon cloth (plain, Fuel Cell Earth), tris(2,2'-bipyridyl)ruthenium(II) chloride hexahydrate (98% Acros Organics), 2-propanol (>99.5%, Fischer Chemical), triethylamine (>99.5%, EMD Millipore Corporation), 8-hydroxypyrene-1,3,6 trisulfonic acid trisodium salt (HPTS, >98%, Carbosynth), methyl iodide (99%, Alfa Aesar), dimethylsulfoxide (>99.9%, fisher chemical), ethyl acetate (>99.5%, Fisher Chemical), acetone (>99.5%, Fisher Chemical), thionyl chloride (>99%, Sigma-Aldrich), *N,N*-dimethylformamide (>99.8%, Macron Fine Chemicals), dichloromethane (>99.5%, Macron Fine Chemicals), 1-boc-ethylenediamine (98%, Combi-Blocks), tetrahydrofuran (>99.9%, Fisher Chemical), acetonitrile (>99.5%, Fisher Chemical), chloroform (99.8%, VWR Chemical BDH), and trifluoroacetic acid

(99%, Oakwood Chemical). Purified 8-hydroxypyrene-1,3,6-tris(2-aminoethylsulfonamide) (HPTSA), as the trifluoroacetate salt, was available from prior work.[36]

Synthesis of Methyoxylated Photoacid, MeOPTSA, as a Negative Control. In a round bottom flask, HPTS (5.0 grams, ~9.6 mmol) was dissolved in 80 mL of dimethylsulfoxide. NaOH pellets (0.50 g, ~12.5 mmol) were added and stirred for 30 min at room temperature. Methyl iodide (2.28 g, ~16 mmol) was added and the solution was stirred for 48 h at room temperature. A yellow crude solid was suspended in solution upon addition of 200 mL of ethyl acetate. The product was filtered using vacuum filtration and rinsed with ethyl acetate (2 x 50 mL) followed by acetone (3 x 50 mL). The final crude product was recrystallized with methanol and water to yield a yellow powder. The recrystallized product was characterized when dissolved in $D_2O(l)$ using ^{1}H-NMR spectroscopy (DRX500, Bruker), as a solid powder after drying under vacuum at $60 - 70$ °C overnight using FTIR–ATR spectroscopy (FT/IR-4700 equipped with ATR-PRO ONE, JASCO), and as an aqueous solution using electronic absorption spectroscopy (Duetta, HORIBA). Spectral features were consistent with the methoxylated photoacid, 8-methoxypyrene-1,3,6 trisulfonate (MeOPTS). Conversion of MeOPTS to its trisulfonamide variant, MeOPTSA, was performed using the protocol that we previously reported for conversion of HPTS to HPTSA,[36] with minor modification that purification was performed using column chromatography (Teledyne ISCO, CombiFlash NextGen 300+).

Covalent and Ionic Bonding of Dyes in Nafion Membranes. Synthesis of PFSA ion-exchange membranes with covalently bound HPTSA and MeOPTSA, and Nafion with ionically associated $[Ru^{II}(bpy)_3]^{2+}$, where bpy is 4,4'-bipyridine, were described in our previous works.[13] Briefly, for covalently bound dye-modified PFSA, a sheet of Nafion precursor poly(perfluorosulfonyl fluoride) was cut into ~3 x 3 cm membranes. The membranes were bathed and stirred in a

scintillation vial filled with 75 µL of 1M NaOH(aq), 45 µL of triethylamine, and the following dye solutions at 90 ℃ for 7 days. For **DSM-H1** and **DSM-H2**, 5 mg HPTSA in 20 mL isopropyl alcohol was used for PFSA modification (>4 OD at 405 nm) while a ten-fold serial dilution of this solution was used to synthesize **DSM-L** with a lower dye density. An arbitrary amount of purified MeOPTSA was directly transferred from column chromatography to 20 mL of isopropyl alcohol for the synthesis of MeOPTSA-modified PFSA due to low yields. For $[Ru^{II}(bpy)_3]^{2+}$ ionically associated into Nafion, a sheet of Nafion NR-212 was cut into ~3 x 3 cm membranes and pretreated by stirring in 1 M H_2SO_4(aq) for 1 h on a stirplate, followed by copious rinsing and storage in deionized water until use. The pretreated membranes were placed in scintillation vials containing 6 mg $[Ru^{II}(bpy)_3]Cl_2$ in 5 mL of 1 M H_2SO_4(aq) and stirred for 36 h at 80 °C using a sand bath. No emphasis was placed on any specific orientation of PFSA during modification or photoelectrochemical measurements.

Absorption and Photoluminescence Spectroscopy. Absorption and photoluminescence spectra were obtained using a spectrometer (Duetta, HORIBA). HPTSA-modified PFSA was mounted in a custom sample holder machined out of KEL-F and similar to H-cells used previously for our photoelectrochemical studies.[13,15] Notable modifications include the use of four glass windows in a rectangular arrangement to allow for in situ probing of right-angle photoluminescence and positioning of the membranes at an angle of 50 degrees relative to the optical axis (**Figure 2a**) to prevent specular reflection of light from the excitation beam directly into the "right-angle" detector. Membranes were placed in-between two parafilm gaskets with slightly oval cutouts, to match the opening in the KEL-F block at 50 degrees. Absorption spectra were baseline corrected using the sample holder filled with ultrapure water in the absence of a sample. Photoluminescence spectra were collected for 400 nm light excitation in a right-angle configuration with 5 nm excitation and

emission slit widths and with resulting data autocorrected for the wavelength-dependent sensitivity of the detection system.

Photoelectrochemical Measurements. Electrochemical measurements were conducted using a potentiostat (VSP-300, Biologic) in a four-electrode configuration consisting of platinum mesh current-carrying electrodes (0.15 cm^2) and Ag/AgCl potential-sensing electrodes. These sensing electrodes were prepared by sanding an Ag wire, rinsing it with dilute nitric acid, and rinsing it with copious amounts of ultrapure water, followed by immersing ~3 cm of the bottom of the clean Ag wires in an aqueous 8.25% sodium hypochlorite generic bleach solution for 15 min. After oxidation, the Ag/AgCl wires were rinsed and aged in ultrapure water overnight. To physically block incident illumination from interacting with the Ag/AgCl wires, a piece of Teflon tubing that was encased in opaque polyolefin heat-shrink was used as a sheath for the Ag/AgCl wires. Membranes were placed in-between two parafilm gaskets with circular cutouts (1.4 cm diameter) to define the geometric membrane active area. Specifically, for the experiment that used carbon cloth affixed to Nafion NR-212, before loading into the parafilm gasket carbon cloth was placed against Nafion that had been cut into ~3 x 3 cm membranes and pretreated by stirring in 1 M H$_2$SO$_4$(aq) for 1 h on a stirplate, followed by copious rinsing and storage in deionized water until use. Each chamber contained 9 mL of aqueous electrolyte that wetted the membrane to form an active area of 1.54 cm^2. Working electrodes were placed in the larger concentration (concentrated) electrolyte chamber for all experiments. The concentrated and dilute electrolyte chambers form the low-impedance charge-collection junction and the rectifying charge-separation junction, respectively. Glass Luggin–Haber capillaries each with a ~1 mm tip diameter were installed ~1 mm from each side of the membrane to minimize potential drop due to uncompensated resistance between the Ag/AgCl sensing electrodes and to physically place the Ag/AgCl wires away from

the path of incident illumination. Polyethylene terephthalate tubes were affixed to the fill ports of our custom H-cell to allow the aqueous electrolyte to remain at a large distance above the cell so that the current-carrying wires could also be positioned out of the path of incident illumination.

Optical excitation was achieved with a continuous-wave laser diode (L405G1, Thorlabs; 405 ± 5 nm) beam expanded to slightly underfill the active area of the membrane. The irradiance was adjusted with a set of neutral density filters and measured with a thermopile detector (S310C, Thorlabs). A monochromatic excitation source was used instead of a white-light source to minimize effects due to heating and, in general, to allow for facile quantification of quantum yields, which are not reported herein. Monochromatic irradiance at 405 nm was converted into equivalent Suns excitation by taking the ratio of the absorbed photon fluence rate for **DSM-H1** at 405 nm and the expected absorbed photon fluence rate of **DSM-H1** under reference air mass 1.5 global solar spectral irradiance,[37] as calculated in previous works.[13,14,38] An equivalent excitation of 1 Sun was determined to be equal to 31.3 mW/cm^2 of 450 nm light. Photoresponse data are reported as the mean of data collected 117.5 s $\pm$ 2.5 s into a 2-min period of illumination versus data in the dark before illumination. After illumination, the system was allowed to return to its pre-illumination state by sitting in the dark for at least 3 min, which is the minimum time needed to reach a quasi-steady-state signal. Each of these processes was controlled by a custom optical shutter.

All membranes were positioned in our custom H-cell containing the desired experimental electrolytes in each chamber and allowed to soak for at least 10 min, followed by exchange of the soaking electrolyte with fresh electrolyte prior to photoelectrochemical evaluation. When an experiment required changing the composition of an electrolyte, e.g. from HCl(aq) to KCl(aq), membranes were submerged in 1 M of the new aqueous electrolyte, with a large enough volume so that electrolyte species were in excess, and stirred overnight, followed by copious rinsing with

deionized water and storage in the lowest concentration experimental electrolyte to be used. V_{oc} values as a function of irradiance were collected by performing three trials under the same experimental conditions, refreshing the electrolyte after each trial, and are reported in reference to the corresponding open-circuit potential (E_{oc}) in the dark, meaning that $V_{oc} = E_{meas} - E_{oc}$, where E_{meas} is the measured potential difference. Negative control experiments were each conducted once using $[Ru^{II}(bpy)_3]^{2+}$ ionically associated into Nafion, carbon cloth affixed to Nafion, and MeOPTSA-modified PFSA. Chronoamperometry measurement used to quantify membrane conductance were performed out of sequence by alternating the polarity of the applied potential bias before increasing the magnitude of the applied potential bias in order to reduce net transport of ions across the membrane.

Transient Absorption Spectroscopy. Kinetics data for the reprotonation of ground-state deprotonated HPTSA(aq) were collected with a custom transient absorption spectroscopy system. Optically dilute aqueous solutions of HPTSA ($Abs_{355nm} < 0.05$ at the excitation wavelength (λ_{ex})) were titrated to pH values of ~3 – 6 using concentrated $HClO_4$(aq). $HClO_4$(aq) was chosen for its high acidity ($pK_a = -10$) and redox stability of the conjugate base, ClO_4^-(aq). Other strong acids, specifically H_2SO_4(aq) ($pK_{a,1} = -3.0$, $pK_{a,2} = +2.0$) and HNO_3(aq) ($pK_a = -1.3$), were avoided to prevent excited-state proton transfer between HPTSA*(aq) and the conjugate base of the strong acid. Titrated solutions were sparged with argon and excited using the third harmonic of an Nd:YAG laser (Continuum Minilite II, ~5 ns pulse width) at 0.6 mJ/pulse and probed with an optically chopped 150 W xenon arc lamp (~2 ms pulse width) with averaged signals obtained from 100 pump–probe pulses. A 360 nm long-pass filter was used for both full spectra and single-wavelength measurements to minimize laser scatter into the monochromator, while a 450-nm short-pass filter was introduced for single-wavelength pH-dependent measurements to attenuate

photoluminescence. To minimize effects due to excited-state species, including competing transient absorption signals and PMT ringing due to strong photoluminescence, kinetic analysis of transient absorption data was performed starting 100 ns after photo-excitation. In order to preserve time resolution at early times, at the expense of signal-to-noise, data was adjacent-average smoothed in a logarithmic time domain resulting in <100 points for each decade of time.

Results and Discussion

Advances and rationale for updated electrochemical setup and protocols. We recently reported photovoltaic action via visible-light excitation of a PFSA membrane covalently modified with HPTSA,[13] an analog of the well-known super-photoacid 8-hydroxypyrene-1,3,6-trisulfonate (HPTS; pyranine) (**Figure 2b**).[16] Observed photocurrent densities were as large as 100 $\mu A/cm^2$, however photovoltages were only ~1 mV. While that work set the benchmark for this new class of functional materials, the experimental setup and protocols used to quantify photovoltaic behavior were imperfect. In particular, the aqueous electrolytes used were far from ideal because they consisted of strong acid (H_2SO_4) separated from strong base (NaOH) by only a cation-exchange membrane (modified Nafion). For protonic photovoltaics based on cation-exchange membranes, it is *detrimental* to use concentrated base to try to maximize chemical potential differences of each mobile charged species, and thus the electric potential difference, across the rectifying charge-separation junction, because it results in unstable acid–base gradients due to opposing transport of H^+ toward the alkaline electrolyte and Na^+ toward the acidic electrolyte. This is evidenced by the magnitude of the net built-in electric potential difference being significantly smaller than that predicted by **Equation 2**, when the concentration of protons on each side of the membrane is used as a surrogate for the activity in the numerator and the denominator of the

reaction quotient fraction. And because Nafion and related cation-exchange membranes exhibit similar abilities to transport H$^+$ and Na$^+$, these conditions suggest that over time there was a substantial loss in the pH difference across the membrane, which was not immediately noticeable due to the large volumes of solution and large concentrations of acid and base used.

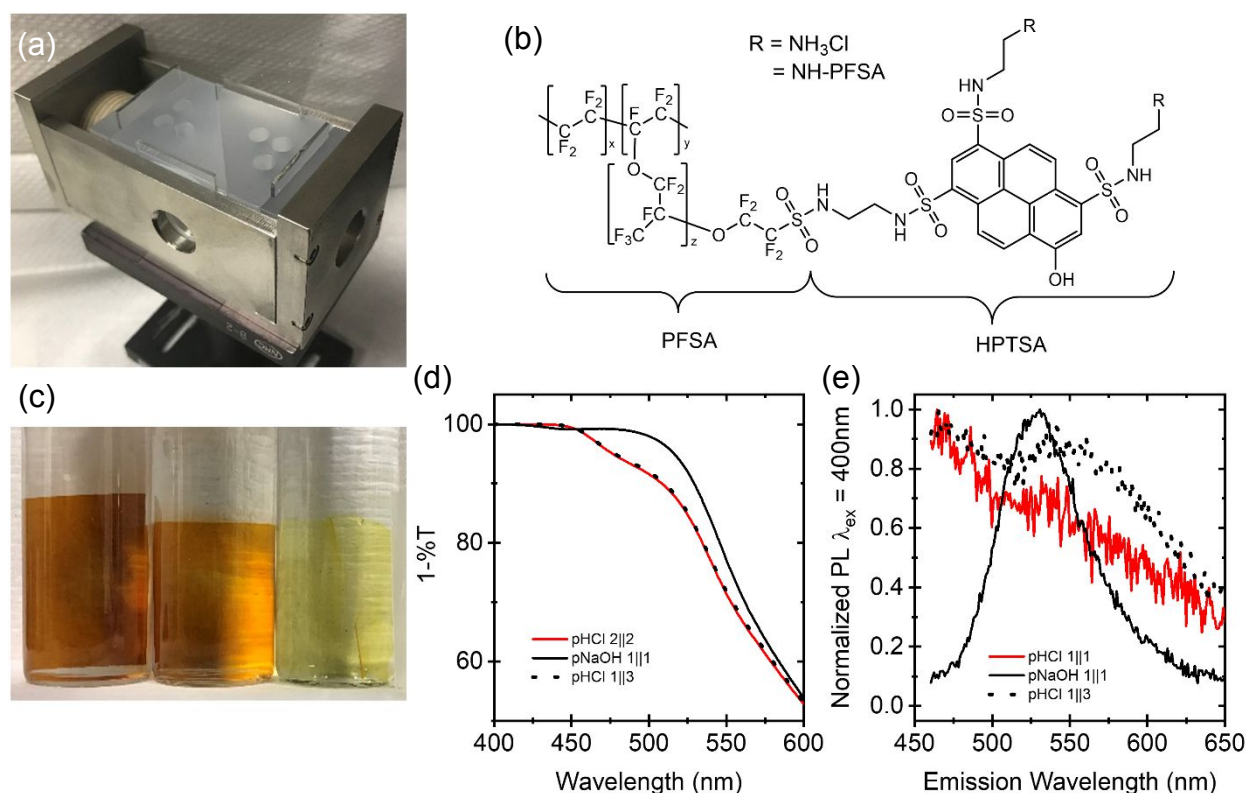Comparatively, for analogous electronic photovoltaic semiconductor constructs, it is

Figure 2. (a) Photograph of custom four-window H-cell used to perform absorption and photoluminescence measurements on wetted samples. **(b)** Chemical structure of HPTSA-modified PFSA. More than one ethylenediamine group can covalently bond to PFSA, as indicated by the two options for each of the R groups, which may result in crosslinking of the polymer membrane. **(c)** Photograph of HPTSA-modified PFSA with, from left-to-right, greatest-to-least concentration of dye (**Table 1**). **(d)** Transmittance spectra and **(e)** normalized photoluminescence spectra for **DSM-H1** (leftmost membrane in **panel c**) under the aqueous pHCl (pNaOH) conditions indicated, where pHCl (pNaOH) stands for "–log [HCl] ([NaOH])" and [HCl] ([NaOH]) is the concentration of HCl (NaOH), such that pHCl 1||3 means 100 mM HCl(aq)||1 mM HCl(aq), and in which case light was incident on, and photoluminescence was detected from, the side with the dilute electrolyte chamber.

beneficial to try to maximize chemical potential differences of each mobile charged species, and thus the electric potential difference, across the rectifying charge-separation junction and it is

beneficial to try to minimize chemical potential differences of each mobile charged species, and thus the electric potential difference, across the low-impedance charge-collection junction. However, for protonic photovoltaics based on cation-exchange membranes it is *detrimental* to use concentrated acid to try to minimize chemical potential differences of each mobile charged species, and thus the electric potential difference, across the low-impedance charge-collection junction. This is because Donnan exclusion, which results in a substantial difference in the concentration of one ion charge type – the coion – over the other ion charge type – the counterion – is poor when the activity of salt species in the contacting aqueous electrolyte is similar to the activity of fixed-charge groups in the ion-exchange membrane. The extent of Donnan exclusion can be approximated by the following equation, which is derived in the Supplementary Information in the subsection titled "Donnan Theory and the Capacity for Ion Exclusion,"

$$\left[\text{Coion}^m_{-/+} \right] = \frac{\left[\text{Salt}^s_{\pm} \right]^2}{\left[\text{Fixed}^m_{-/+} \right]} \tag{5}$$

where $\left[\text{Coion}^m_{-/+} \right]$ is the coion anion (cation) concentration in a cation-exchange (anion-exchange) membrane (m), $\left[\text{Salt}^s_{\pm} \right]$ is electrolyte salt concentration in solution (s), and $\left[\text{Fixed}^m_{-/+} \right]$ is the concentration of fixed negatively-charged (positively-charged) groups in a cation-exchange (anion-exchange) membrane.[27] When $\left[\text{Salt}^s_{\pm} \right] \geq \left[\text{Fixed}^m_{-/+} \right]$, $\left[\text{Coion}^m_{-/+} \right] \approx \left[\text{Salt}^s_{\pm} \right]$ and thus no Donnan exclusion exists across the interface, resulting in poor permselectivity based on ion charge type. Nafion NR-212 has $\left[\text{Fixed}^m_{-/+} \right] \approx 1$ M,[39,40] which is approximately the value that we determined for both Nafion NR-212 and our modified Nafion membranes based on measurements of ion-exchange capacity in our prior work.[13] Since we used aqueous 1 M H_2SO_4 and 1 M NaOH electrolytes in our prior work,[13,15] this meant that Donnan exclusion was poor and that SO_4^{2-} and

OH$^-$ coions were likely present in the modified Nafion membranes at concentrations in the hundreds of millimolar range, or larger.[41]

When different concentrations of salt species are present in each aqueous electrolyte that wets an ion-exchange membrane, the concentration of partially Donnan excluded coions in the membrane, and their associated mobile counterions, differs at each membrane|solution interface, resulting in diffusion of neutral electrolyte species down its concentration gradient and ultimately formation of a steady-state liquid-junction (LJ) electric potential difference (ϕ_{LJ}^{mem}) across, but within, the membrane (mem). Therefore, similar to electric potentials across pH probes,[42] electric potentials across ion-exchange membranes consist of at least three contributions (2 ϕ_D^{int} (**Equations 1 and 2**) and 1 ϕ_{LJ}^{mem}), where the presence of a nonzero value for ϕ_{LJ}^{mem} is indicative of ion crossover and means that the system has not reached electrochemical equilibrium. Ion crossover can be further slowed, even to the point of $\phi_{LJ}^{mem} = 0$, when a membrane affords additional means for selectivity of one charge type over the other. For example, perfect ion selectivity is thought to be possible when extremely large polyelectrolyte counterions are used, because size exclusion prevents them from existing as coions in the ion-exchange membrane or using pinhole-free monolayer materials like graphene and boron nitride, because they only allow for transport of H$^+$ via quantum mechanical tunneling.[43,44] In these cases, the processes and outcome of forming interfacial space–charge regions to modulate ion-transport properties are identical to those that occur at interfaces of solid-state electronic semiconductors to modulate electron-transport properties.

We synthesized three ion-exchange membranes consisting of HPTSA covalently bound to PFSA at various photoacid dye binding densities using a previously reported procedure[13] (**Figure 2c,d**, **Table 1**): two samples contained a high concentration of photoacid dyes (**DSM-H**) and one

sample contained a low concentration of photoacid dyes (**DSM-L**). To obtain electric potential differences that were stable on the timescale of days with only minor evidence for ion crossover, we only used acidic electrolytes to wet each side of the membrane and decreased the acid concentration that we used previously from 1 M to between 100 mM HCl(aq) (pHCl = 1) and 0.1 mM HCl(aq) (pHCl = 4). Unless stated otherwise, from this point forward we define pHCl to stand for "–log [HCl]," where [HCl] is the concentration of HCl, and not "–log a_{HCl}," where a_{HCl} is the activity of HCl. Using sub-molar concentrations of aqueous HCl resulted in improved Donnan exclusion, with projected concentrations of Cl$^-$ coions in the modified Nafion membrane in the single millimolar to nanomolar ranges. While these modifications to the experimental design resulted in significant attenuation of rates of salt crossover, as well

Table 1. HPTSA-modified PFSA membranes with various dye doping densities as indicated by optical densities (OD) at 405 nm.

Membrane	OD$_{405\ nm}$
DSM-H1	>4
DSM-H2	>4
DSM-L	0.664

as somewhat improved accuracy of Donnan theory and **Equation 2** to predict net built-in electric potential differences across the membrane (**Figure S1a**), these modifications also generated new challenges. First, any measurements of current were now strongly limited by uncompensated resistance between the sensing electrodes and the membrane interface, so much so that Luggin–Haber capillaries could not remedy this limitation (**Figure S2**). Therefore, the magnitude of photocurrent values were not representative of the applied potential to HPTSA-modified PFSA. This suggests that detailed analysis of photocurrent values is futile, while also supporting the observation that light and dark current density *versus* potential data are linear, even when ion-exchange-membrane–liquid junctions were designed for effective current rectification and charge separation. Second, typical reference electrodes could not be used because salt leaked from the saturated salt solution in the fritted tubes into the electrochemical cell, which resulted in dynamic

interfacial equilibration and unstable E_{oc} values on the timescale of ~1 h (**Figures S3**). To remedy this latter challenge, double-junction reference electrodes and commercially available so-called leak-free reference electrodes were evaluated but still determined unsuitable for our work because of their less accurate values for E_{oc} than measured using Ag/AgCl wires, especially in solutions with low ionic strength (**Table S1**). Therefore we decided to use Ag/AgCl wires immersed directly into the aqueous HCl electrolytes as potential-sensing electrodes and shielded from direct interaction with light incident from the illumination source (**Figure S4**), because Ag/AgCl is known to be photoactive.[45] This resulted in E_{oc} values that were *stable on the timescale of days*, and even allowed us to observe minor effects due to osmosis over that timescale (**Figure S5**).

A critical constraint imposed by use of immersed Ag/AgCl wires as potential-sensing electrodes is exclusive use of chloride-containing electrolytes and reported electrode potential differences that are sensitive to not only net electric potentials across the membrane, but also differences in the activity of Cl⁻(aq). An advantage to this setup is that the sign of ϕ_D^{mem} is such that $\Delta\bar{\mu}_{Cl} = \Delta\mu_{Cl} + zq\phi \neq 0$, and because the Ag/AgCl wires are sensitive to $\Delta\bar{\mu}_{Cl}$, this results in a non-zero value for the open-circuit potential, E_{oc}. If an anion-exchange membrane had separated the two sides of the electrochemical cell or the Ag/AgCl wires had been replaced with reversible hydrogen electrodes, then the sign of ϕ_D^{mem} would have led to near-zero E_{oc} values and provided little information about the value of ϕ_D^{mem}.[46] These facts are apparent by analyzing E_{oc} as follows, which is rigorously derived using electrochemical potentials[47] in the Supplementary Information in the subsection titled "Electric Potential Differences Measured using Ag/AgCl Wires,"

$$E_{oc} = E_N^{redox} + \Sigma\phi_i = \left\{E_N^{int,WE} + \left(-E_N^{int,CE}\right)\right\} + \left\{\left(\phi_D^{int,WE}\right) + \left(-\phi_D^{int,CE}\right)\right\} + \phi_{LJ}^{mem} \quad (6)$$

where ϕ_i is any contribution to differences in electric potential between nearer to the WE *versus* nearer to the CE, including Donnan potentials, **Equations 1 and 2**, and liquid-junction potentials. Using **Equations 3 and 4**, and assuming a position-independent formal reduction potential because both sensing electrodes are the same type, $E_N^{o',int,WE} = E_N^{o',int,CE}$, E_{oc} can be rewritten as follows,

$$E_{oc} = \left\{ \frac{RT}{F} \ln \frac{[Cl^-]^{CE}}{[Cl^-]^{WE}} \right\} + \left\{ \frac{RT}{F} \ln \frac{[H^+]^{CE}}{[H^+]^{WE}} \right\} + \phi_{LJ}^{mem} \tag{7}$$

$$E_{oc} = \frac{2RT}{F} \ln \frac{[HCl]^{CE}}{[HCl]^{WE}} + \phi_{LJ}^{mem} \tag{8}$$

$$E_{oc} = 2\phi_D^{mem} + \phi_{LJ}^{mem} \tag{9}$$

The final expression results from use of **Equation 2**, and the fact that for each solution [HCl] = [H⁺] = [Cl⁻], and therefore every concentration term can be replaced with [HCl]. **Equation 9** indicates that when E_{oc} is measured across a *cation*-exchange membrane using sensing electrodes whose reduction products, e.g. Cl⁻(aq), are equal to the concentration of cations in the electrolyte, the net effect is a non-zero E_{oc}. And assuming that ϕ_{LJ}^{mem} is small,[42] the net Donnan membrane potential, ϕ_D^{mem}, can be deconvoluted from measured E_{oc} values in the dark as $\phi_D^{mem} \approx E_{oc}/2$. Moreover, we assume that under illumination, $\Delta E_{oc} = V_{oc} \approx \Delta\phi_D^{mem}$, which implies that only changes in electric potential are detected at the potential-sensing electrodes, and not changes in chemical potential of Ag, AgCl, and/or Cl⁻, and thus not E_N^{int} at an electrode|solution interface. We assume this to be true, because generally the activity of Cl⁻ should not be altered by the photoacid dye sensitization Förster cycle. In addition, steady-state V_{oc} values are observed after only a short ~2 min illumination time and distances that Cl⁻(aq) must transport in order to influence E_N^{int} at the Ag/AgCl wires, 2.5 cm from membrane to electrode, are ~500 times larger than the maximum

distance that Cl⁻(aq) must transport to influence either value of ϕ_D^{int} at a membrane|solution interface, <50 μm across the membrane.
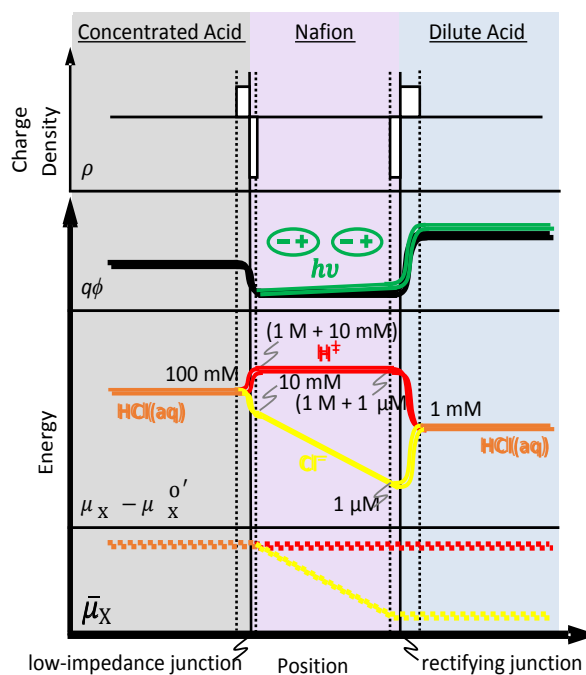

Figure 3. Spatial representation, from top to bottom, of near-equilibrium uncompensated charge density; electric potential as an energy; chemical potentials each referenced to its concentration chemical potential (where "concentration" is commonly used for equilibrium constants and is analogous to "formal" for reduction potentials) and including concentrations of mobile charged species, X = H⁺ or Cl⁻; and electrochemical potentials, each expected for wetted Nafion|solution interfaces. Also shown in green is the proposed outcome of continuous-wave illumination, where dipoles are proposed to form at steady state that results in an increase in the magnitude of the membrane potential from values measured in the dark.

Effects of junction contacts on electric potential differences in the dark and light. It is useful to quantify net electric potential differences across semiconducting devices, because those values are predictive of the ability of the device to rectify current well and exhibit large values for V_{oc}. Validation of variable-magnitude built-in membrane potentials was achieved by wetting HPTSA-modified PFSA on each side by different concentrations of aqueous acidic electrolytes: moderate acid on one side, e.g. pHCl = 1 − 2, and weaker acid on the other side, e.g. pHCl = 3 − 4, with an example projected distribution of ions for pHCl 1‖3 across Nafion shown in **Figure 3**. Unlike in electronic semiconductor–liquid-junction photoelectrochemical constructs, ion-exchange membranes in contact with aqueous electrolytes are limited to approximately a 2–3-unit pH difference across the membrane due to limitations described above. As expected, using our new more accurate setup and protocols, HPTSA-modified PFSA exhibited values of E_{oc} that are similar to those predicted by Donnan theory (**Table 2**), suggesting that the bulk material is still a cation-exchange membrane even at the largest loading of photoacid molecules used, which are proposed to covalently bind to sulfonate groups and therefore decrease protonic dopant density.[13] Differences between measured E_{oc} values and those predicted by Donnan theory were largest in magnitude, resulting in the largest predicted values for ϕ_{LJ}^{mem}, when the low-impedance junction was in contact with the chamber that contained a large concentration of aqueous electrolyte, i.e.

Table 2. Open-circuit potential (E_{oc}, in mV) and open-circuit photovoltage (V_{oc}, in mV), under 405 nm illumination at 1.4 Suns equivalent excitation (45 mW/cm^2 of 405 nm laser light) measured across **DSM-H1** for different combinations of HCl(aq) concentrations in contact with the membrane to form the low-impedance junction (first value; larger concentration; at working electrode (WE)) and the rectifying junction (second value; smaller concentration; at counter electrode (CE)), calculated values (in mV), and differences (in mV) attributed to ϕ_{LJ}^{mem}.

pHCl condition	E_{oc} (measured)	ϕ_D^{mem} (calculated using **Equation 2**, with T = 25 °C, approximately ambient)	ϕ_{LJ}^{mem} (calculated using **Equation 9**)	V_{oc} (measured)
2‖3	-113.7 ± 0.3	-59.2	+4.7 ± 0.3	-0.19 ± 0.02
2‖4	-229.1 ± 0.3	-118.4	+7.7 ± 0.3	-0.78 ± 0.01
1‖2	-109.3 ± 1.4	-59.2	+9.1 ± 1.4	-0.58 ± 0.07
1‖3	-219.1 ± 0.6	-118.4	+17.7 ± 0.6	-2.2 ± 0.2

100 mM HCl(aq) (pHCl = 1), and/or when the rectifying junction was in contact with the chamber that contained the smallest concentration of aqueous electrolyte, i.e. 0.1 mM HCl(aq) (pHCl = 4). Despite the existence of Donnan exclusion of Cl^- coions, the cause of these large values for ϕ_{LJ}^{mem} are likely due to the presence of a relatively large concentration of Cl^- coions immediately inside the membrane in contact with the concentrated electrolyte that results in substantial rates of HCl crossover and/or significant changes in local HCl concentration in the dilute electrolyte near the membrane, respectively.

Using our new more accurate setup and protocols, we now observed that illumination results in an *increase* in the magnitude of E_{oc}, and thus an increase in the net electric potential difference between nearer to the WE *versus* nearer to the CE. This results in the *sign* of V_{oc} values (**Table 2**) being opposite ("reverse") of those expected if the same electrostatic distributions had existed in solid-state electronic semiconductor pn-junction or Schottky junction solar cells and opposite of our previous observations using significantly larger concentrations of aqueous acidic electrolyte.[13,15] Nevertheless, "reverse" photovoltaic action has been reported previously in the literature for electronic solar cells[48–53] and for bipolar-membrane-based light-driven proton pumps,[54] often proposed to occur due to dynamic processes that are common in soft polymer materials like ion-exchange membranes. Irrespective, the *magnitude*, on the order of 1 mV, and *timescales*, on the order of 1 min, of growth and decay for our observed quasi-steady-state "reverse" V_{oc} values are each rather similar to those we reported previously,[13,15] and again were *independent on the direction of illumination* (**Figure S6**), suggestive of a bulk photovoltaic mechanism.

Solar cells based on electronic semiconductors exhibit larger values for V_{oc} when they have a low-impedance charge-collection junction, with a small magnitude built-in electric potential

difference, and a highly rectifying charge-separation junction, with a large magnitude built-in electric potential difference. To determine whether these same design rules exist for HPTSA-modified PFSA, E_{oc} values and V_{oc} values were examined for various combinations of electrolyte concentrations in the concentrated and dilute electrolyte chambers (**Table 2**) and as a function of irradiance (**Figure 4**). V_{oc} values correlate somewhat well to E_{oc} values, which are dominated by Donnan-potential-induced membrane–liquid junctions, but correlate even better with minority contributions to E_{oc} presumably due to liquid-junction potentials, ϕ_{LJ}^{mem}, therefore suggesting that crossover of HCl may be a related to the observed photovoltaic behavior. Comparing conditions when the electrolyte concentration used to form the low-impedance junction is the same (**Figure 4a**, black *versus* red, and green *versus* blue), V_{oc} values are largest when an electrolyte with a *larger* value for pHCl is in contact with the rectifying junction, leading to a larger magnitude net built-in electric potential difference. When the electrolyte concentration used to form the rectifying junction of the same (red *versus* green), V_{oc} values are largest when an electrolyte with a *smaller* pHCl is in contact with the low-impedance junction, leading to a smaller impedance for charge collection. This suggests that the overarching design principle for efficient charge separation and charge collection in our protonic membrane–liquid-junction assemblies is to use electrolytes with a large difference in pHCl, and thus protonic chemical potential, across the membrane and large values for ϕ_{LJ}^{mem}. The former condition is analogous to the design principle in electronic semiconductor–liquid-junction photoelectrochemical constructs where a large difference in reduction potential, and thus electronic chemical potential, is desired. However, for our protonic membrane–liquid-junction assemblies, the magnitude of the net electric potential difference increases upon illumination resulting in "reverse" photovoltaic action, not decreases as would be expected for traditional electronic semiconductor–liquid-junction designs. Moreover, the fact that

DSM-L, which contained an order-of-magnitude less photoacids, exhibited a slightly larger value for its maximum V_{oc} than **DSM-H1** and **DSM-H2** (**Figure 4b**) suggests that photochemical performance benefits from polymer morphologies present when photoacid concentrations are smaller[55] and/or when photoexcitation is more homogenous.

Effects of dye photochemistry and photophysics on electric potential differences in the light. As desired, illumination of HPTSA-modified PFSA results in photoacids undergoing the dye sensitization Förster cycle, which is supported by the presence of small photoluminescence
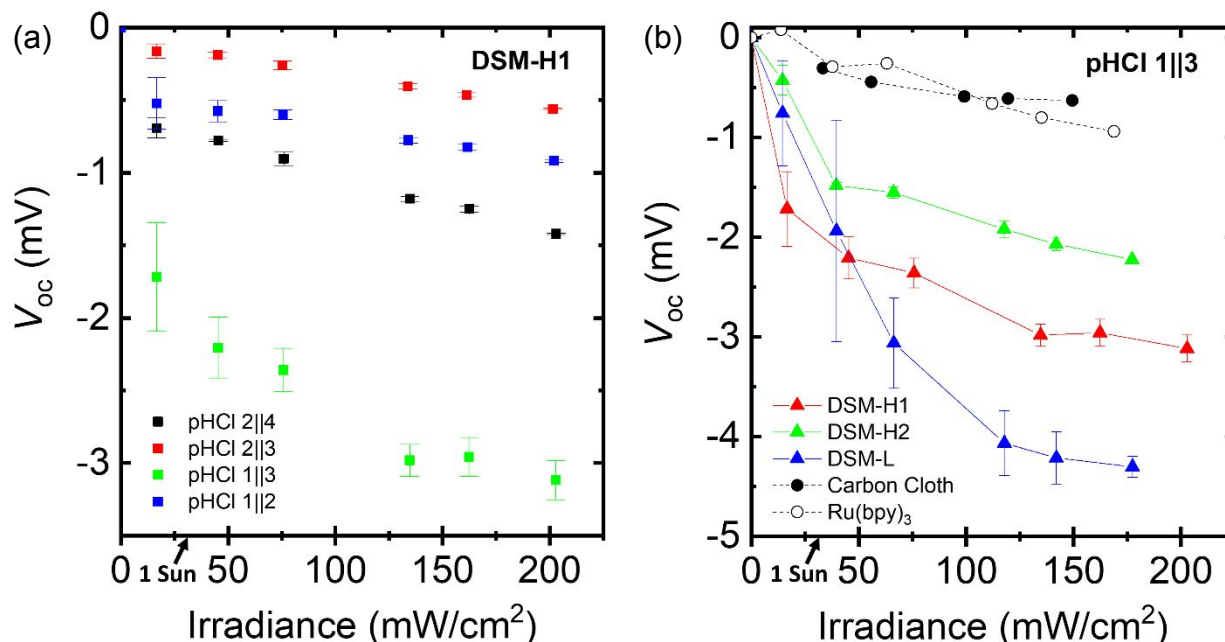
Figure 4. (a) Open-circuit photovoltage (V_{oc}) as a function of irradiance from 405 nm laser light measured across **DSM-H1** for different combinations of HCl(aq) concentrations in contact with the membrane to form the low-impedance junction (first value; larger concentration; at working electrode) and the rectifying junction (second value; smaller concentration; at counter electrode). We define pHCl to stand for "–log [HCl]", where [HCl] is the concentration of HCl, such that pHCl 2||4 means 10 mM HCl(aq)||0.1 mM HCl(aq). **(b)** V_{oc} as a function of irradiance measured across Nafion membranes containing various photoabsorbers under conditions of 100 mM HCl(aq)|| 1 mM HCl(aq) (pHCl 1||3). HPTSA ("**DSM**" datasets) was covalent bound to PFSA, [$Ru^{II}(bpy)_3$]$^{2+}$ was ionically associated into commercial Nafion NR-212, and carbon cloth was affixed to one side of commercial Nafion. Optical densities at 405 nm were >4, except for **DSM-L**, which was 0.664. Data and error bars for each **DSM-X** are the mean ± standard deviation of three trials while each negative control measurement was only performed once. The condition of 1 Sun equivalent excitation occurs for an irradiance of 31.3 mW/cm^2.

features that resemble those from deprotonated HPTSA (**Figure 2e**). In addition, because >75%

of excited-state photoacids recombine non-radiatively independent of their protonation state,[36]

absorption of incident illumination necessarily results in significant local heating, which may

influence rates of species transport and reactivity. Because **DSM-H1** and **DSM-H2** each has an

optical density at 405 nm of >4 OD, illumination predominantly heats the side of the membrane

that the light was incident on and results in a predictable temperature gradient and expected sign

of V_{oc} due to the Seebeck effect. However, we observed that the *sign* of V_{oc} did not depend on the direction of illumination (**Figure S6**), suggesting that the Seebeck effect was not the main contributor to the observed photoresponse. Notwithstanding, as negative controls two photo-absorbing membranes were evaluated under the optimal pHCl condition of 1‖3 to discern the non-photoacidic contribution to the observed photovoltage (**Figure 4b**): $[Ru^{II}(bpy)_3]^{2+}$, where bpy is 4,4'-bipyridine, ionically associated into Nafion NR-212 ($[Ru^{II}(bpy)_3]^{2+}$/Nafion) and carbon cloth affixed to Nafion NR-212, each with an optical density at 405 nm of >4. Under these conditions, a significant difference between photoacidic and non-photoacidic membranes was apparent (**Figure S7**), suggesting that at least a portion of the photovoltage from HPTSA-modified PFSA is from photoacidic generation of mobile charged species. Moreover, $[Ru^{II}(bpy)_3]^{2+}$/Nafion produced inconsistent values for V_{oc} over time in comparison to **DSM-H1 (Figure 8a,b)**, further supporting the importance of photoacidic behavior in order to observe relatively large values for V_{oc} and suggesting that $[Ru^{II}(bpy)_3]^{2+}$/Nafion is not an ideal negative control for a molecular non-photoacidic photoabsorber. In fact, it has been previously reported that ligands from $[Ru^{II}(bpy)_3]^{2+}$ exchange with solvent molecules under visible-light excitation, with the dissociation rate accelerated in highly acidic environments,[56] calling its stability into question.

Prior literature has reported that intense ultraviolet illumination of HPTS, a precursor of HPTSA, results in its photooxidation.[57] Therefore, to evaluate whether a similar process could also be responsible for some of the observed V_{oc} values from HPTSA-modified PFSA, 1 mM $Fe(ClO_4)_x$(aq), where x is the oxidation state of iron, was introduced into both electrolytes of the pHCl 1‖3 condition to attenuate photooxidation of HPTSA or provide a scavenger for solvated radicals. The addition of iron salts did not result in a significant change to V_{oc} values (**Figure S8c**). Moreover, a methoxylated version of HPTSA, MeOPTSA, was synthesized and characterized

(**Figures S9 and S10**), and when covalently bonded to PFSA and evaluated under conditions of pHCl 2∥3 was shown to exhibit V_{oc} values that were significantly smaller in magnitude and opposite in sign to those observed from HPTSA-modified PFSA (**Figures S11 and S12**), again supporting the importance of photoacidic behavior in order to observe relatively large values for V_{oc}.

Mechanism of photoacid dye sensitization Förster cycle. In efficient photochemical energy conversion devices, photoexcitation results in a change in the concentration of at least two chemical species. Photo-induced processes that occur after light is absorbed by semiconductors and electron-transfer dye sensitizers are well known. In traditional crystalline electronic semiconductors, the extent of occupancy of both conduction-band states (electrons) and valence-band states (holes) change under illumination, while in dye-sensitized solar cells, illumination results in a change in the concentration of semiconductor charged species and in the speciation of redox-active molecules in the liquid electrolyte. Analogous to this, ionic solar cells also benefit from exhibiting a light-driven change in the concentration of two mobile charged species, notably
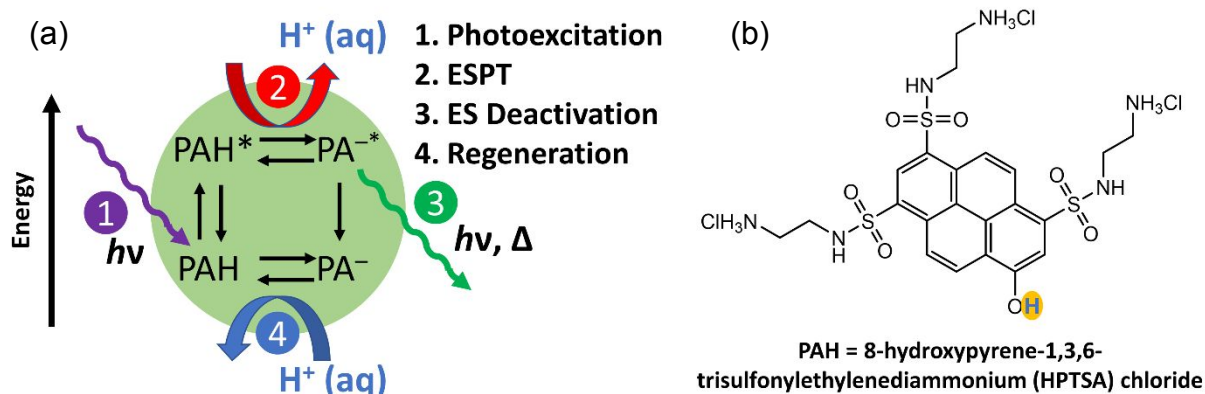

Figure 5. (a) Scheme depicting the photoacid dye sensitization Förster cycle for excited-state proton transfer (ESPT) from HPTSA (PAH), including the predominant aqueous proton acceptor species ($H_2O(l)$) and proton donor species ($H^+(aq)$). **(b)** Chemical structure of membrane-linkable photoacid, HPTSA.

H^+ and OH^- for protonically semiconducting water. This process is enabled through use of

reversible photoacids or photobases, which under specific conditions are hypothesized to generate both H$^+$ and OH$^-$ as an outcome of the dye sensitization Förster cycle (**Figure 5a**).[58] The Förster cycle represents a thermodynamic square scheme for photo-induced proton transfer that is used to approximate the Brønsted–Lowry acidity of photoacids and photobases in their ground state and excited state.[59] It includes several assumptions that limit its applicability for some excited-state proton transfer reactions, such as it assumes that kinetics of proton transfer do not limit excited-state behavior, which is a reasonable assumption for HPTSA and its analogs.[60]

While the Förster cycle serves as a dye-centric representation of the protonation states of photoacidic and photobasic dyes, it does not indicate the transient speciation of water species, which is critical in assessing the ability of a dye to exhibit substantial protonic photovoltaic action. While it is well-known that photoexcitation of super photoacids, like HPTS and its analogs like HPTSA (**Figure 5b**), result in photogeneration of H$^+$(aq) from their excited states,[61] less is known about the protonic speciation that occurs upon regeneration of the ground-state conjugate base of photoacids through reprotonation, via the following reactions,

$$PA^- + H_2O(l) \underset{k_{-1}}{\overset{k_{+1}}{\rightleftarrows}} PAH + OH^-(aq) \tag{10}$$

$$PA^- + H^+(aq) \underset{k_{-2}}{\overset{k_{+2}}{\rightleftarrows}} PAH \tag{11}$$

where PA$^-$ and PAH stand for ground-state deprotonated and protonated photoacids, respectively. When H$_2$O(l) is the proton donor, OH$^-$(aq) is formed, which is desired to obtain substantial photovoltages. However, when H$^+$(aq) is the proton donor then the sensitization cycle produces no net chemical species, suggesting that the photovoltaic effect will be quite small, although

nonzero.[62] As such, we utilized nanosecond transient absorption spectroscopy to quantify and analyze the reaction kinetics and overall behavior of HPTSA dissolved in aqueous electrolytes.

Our time-resolved spectroscopic data (**Figure 6**) suggest sub-nanosecond photogeneration of ground-state deprotonated photoacids and via Steps 1 − 3 in **Figure 5a**, followed by slower nanosecond-to-microsecond regeneration of ground-state deprotonated photoacids via Step 4 in **Figure 5a**. Consistent with Step 4, the transient absorption growth at 480 nm and bleach at 420 nm correspond to near-stoichiometric generation of ground-state deprotonated HPTSA and loss of ground-state protonated HPTSA, respectively (**Figure 6a**). Transient absorption data over time follow a kinetic rate law that is first order in the concentration of deprotonated photoacids (**Figure 6b-f**) and depend significantly on the pH of the solution, with a rate constant that is directly correlated with the activity of $H^+(aq)$, a_{H+}, and with pH defined as "$-\log a_{H+}$." The range of pH values investigated was limited to ~3 − 6 because at pH ≤ 3, transient absorption kinetics due to ground-state reprotonation were indistinguishable from photoluminescence kinetics, suggesting that the rate of Step 4 was similar to, or faster than, the rate of Step 3. Because protonated HPTSA is required to undergo the Förster cycle, the maximum pH used of 5.5 was limited by the pK_a of HPTSA, which we determined to be 4.9 using an acid–base titration procedure with spectrophotometric detection (**Figure S13**), and is consistent with values reported previously.[36] The slowest measured regeneration process occurred at pH = 5.5 and was apparent on the timescale of 10 μs. While at first it may seem unexpected that protonation of a deprotonated molecule in water would require such a long time, this observation is completely consistent with prior observations of proton-transfer processes to and from water.[63–65] Although proton transfer from $H^+(aq)$ to ground-state deprotonated HPTSA is thermodynamically favored with a rate constant that is approximately diffusion limited, mass action applied to **Reaction 11** indicates that the

bimolecular rate can be quite slow at pH $\geq$ 5 due to the presence of $\leq 10^{-5}$ M H$^+$(aq). Moreover,
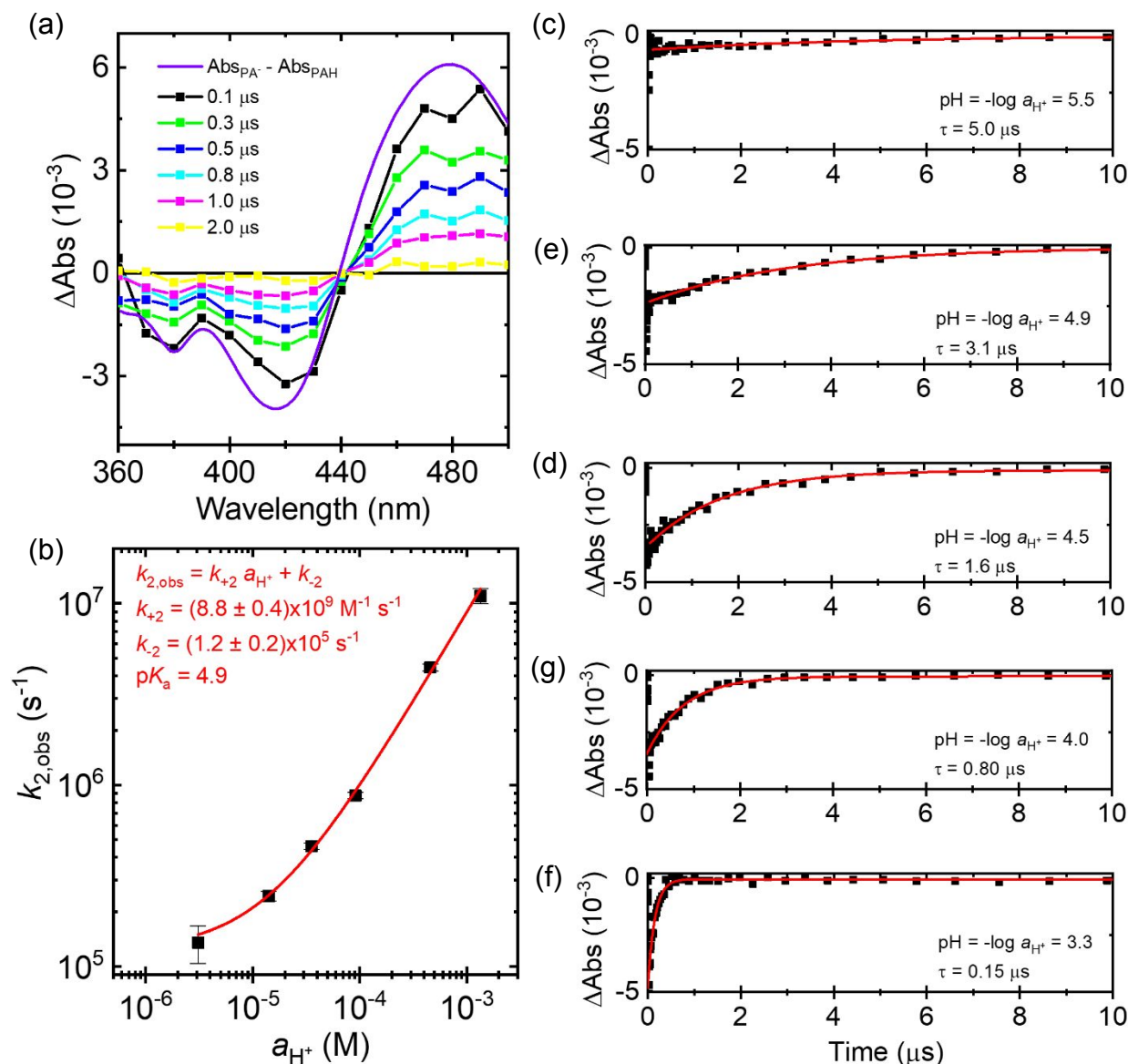
Figure 6. Transient absorption spectroscopy data for HPTSA dissolved in aqueous electrolytes after 355 nm pulsed-laser excitation (0.6 mJ/pulse): **(a)** Transient absorption spectra that resolve the ground-state reprotonation of deprotonated HPTSA. **(b)** Log–log plot of the observed rate constants as a function of the proton activity (a_{H^+}) and a linear least-squares best-fit to obtain the values shown for the second-order rate constant for reprotonation, k_{+2}, and first-order rate constant for deprotonation, k_{-2}. The observed rate constants were determined from non-linear least-squares best fits of the transient absorption data at 420 nm shown in **panels c – f** to a single-exponential decay function with a variable long-time value. Error bars shown in **panel b** represent the standard error of the mean of the pseudo-first-order rate constants from the non-linear least-squares best fits.

because $H_2O(l)$ has $pK_a = 14$, protonation of species with $pK_a < 14$, such as HPTSA, via **Reaction**

10 is thermodynamically unfavored, thus requiring a kinetic barrier at least as large as the standard

Gibbs free energy difference between deprotonation of HPTSA and water, ΔG^o, as follows,

$$\Delta G^{\neq}_{min} \geq \Delta G^{\circ} = 2.303\ RT\ \Delta pK_a \tag{12}$$

where $\Delta G^{\neq}_{min}$ is the minimum activation Gibbs free energy and ΔpK_a is a representation of the difference in acidity between ground-state HPTSA and water. Given that $pK_a \approx 5$, regeneration of ground-state deprotonated HPTSA through deprotonation of water should be quite slow ($>100\ \mu s$) even if one assumes a barrierless back reaction and the fastest frequency factor possible of $\sim 10^{13}$ s^{-1}. Because our transient absorption signals persisted for an order-of-magnitude less time than this projected lower-limit time constant, it is unlikely that desired **Reaction 10** is operative during the dye sensitization Förster cycle for HPTSA(aq).

The observation of a first-order rate constant, k_{obs}, that varies as a function of pH is consistent with reprotonation of ground-state HPTSA following a rate law that is dependent on the activity of H^+(aq), a_{H+} (**Figure 6b**), such as undesired **Reaction 11**. Therefore, these rate constants were analyzed using the following equation,

$$k_{obs} = k_{+2} \cdot a_{H+} + k_{-2} \tag{13}$$

which is derived in the Supplementary Information in the subsection titled "Transient Dye Characterization" based on a model that allows for ground-state dyes to be present in equilibrium between two states prior to photoexcitation.[66] The coincidence of the linear least-squares best fit to the data shown in **Figure 6b** suggests that reprotonation of HPTSA is pseudo-first order, because a_{H+} changes little during the experiment given the low energies used for pulsed-laser excitation, which is consistent with transient absorption studies reported previously for HPTS.[64] Best fits to **Equation 13** not only enable one to obtain the second-order rate constant for reprotonation of ground-state HPTSA from the slope of the best-fit line, $k_{+2} = 8.8 \pm 0.4 \times 10^9\ M^{-1}\ s^{-1}$, but also the first-order rate constant for deprotonation of ground-state HPTSA from the y-intercept of the best-

fit line, $k_{-2} = 1.2 \pm 0.2 \times 10^5$ s^{-1}. The calculated value of k_{+2} is consistent with diffusion-limited recombination between H$^+$(aq) and a somewhat bulky proton-accepting molecule,[67] and the ratio of the rate constants equals K_a, and thus predicts a pK_a value of 4.9, which is consistent with the pK_a value obtained from measurements using a standard acid–base titration procedure (**Figure S13**). Data obtained at pH values significantly greater than the pK_a of HPTSA were excluded from the best fit to **Equation 13**, because the presence of large equilibrium concentrations of deprotonated HPTSA and large pH values resulted in deviations from the pseudo-first-order approximation for H$^+$(aq) and resulted in data that did not fit the trend.

An alternative explanation for **Equation 13** being able to sufficiently fit the data shown in **Figure 6b** is that both **Reactions 10 and 11** are operative, and that nearly all photoacids are protonated prior to pulsed-laser excitation. This would result in an expression for k_{obs} that is identical in form to that of **Equation 13**. However, this is not the case herein because ground-state absorption spectra clearly indicate that up to 80% of HPTSA are deprotonated in their ground state at the largest pH value studied of 5.5 (**Figure S13**). Moreover, based on the calculated pK_a value of HPTSA (4.9) and the pK_a of H$_2$O (14), the largest possible value for the rate constant of **Reaction 10** in the forward direction, k_{+1}, calculated using **Equation 12** and the lower-limit time constant (>100 μs)$^{-1}$, is at least one order-of-magnitude smaller than the y-intercept of the best-fit line in **Figure 6b**.

Collectively, these transient absorption data suggest that reprotonation of ground-state HPTSA with H$^+$(aq) (**Reaction 11**) is significantly faster than reprotonation of ground-state HPTSA with H$_2$O(l) to form OH$^-$(aq) (**Reaction 10**), and thus **Reaction 10** contributes little-to-nothing toward dye regeneration, especially at the pH ≤ 4 conditions used for the photoelectrochemical measurements. Because HPTSA*(aq) is known to only release H$^+$(aq),[60] this

suggests that the only species transiently photogenerated during the dye sensitization Förster cycle that can be collected to perform useful work are H^+, concomitant with formation of polymer-bound deprotonated HPTSA. This implies that upon completion of the dye sensitization Förster cycle zero net chemistry has occurred, meaning that our prior cartoons of processes possible from HPTSA, and related analogs, do not likely depict the dominant reactions in practice.[13,14] This conclusion is of critical importance because the V_{oc} of solar-energy-conversion devices benefits most from light-driven changes in the concentration of minority-carrier species, where small changes in their concentration result in large changes in their chemical potential, which are directly related to the amount of useful work they are able to perform. Since HPTSA is only a photoacid at pH values near or smaller than its measured pK_a value of 4.9, and at these pH values HPTSA*(aq) only releases H^+(aq) and ground-state deprotonated HPTSA(aq) only reacts with H^+(aq), little-to-no minority-carrier OH^-(aq) are photogenerated. In the absence of photogenerated minority-carrier species, V_{oc} values are expected to be small, as we observed herein and previously.[13,15] Moreover, results from these photochemical analyses suggest that HPTSA and its analogs are not optimal for use in photovoltaic light-to-ionic energy conversion processes that mimic traditional electronic semiconductor designs. Detailed numerical[58] and experimental[68] studies of the design guidelines for photoacids and photobases that photogenerate both H^+(aq) and OH^-(aq) to allow for large V_{oc} values indicate that more extreme pK_a and pK_a* values are needed. Reported syntheses and characterizations of such molecules seem to be devoid from the peer-reviewed literature and so we are working to develop new photoacid and photobase motifs that will be far more effective at exhibiting protonic photovoltaic action.

Proposed mechanism for light-to-ionic power conversion. Nafion membranes wetted by aqueous acidic electrolytes have H^+ as counterions to their ~1 M sulfonate groups,[40] meaning that pH ≈ 0 in their bulk quasi-neutral regions.[41] This is relevant because under these nearly super-acidic electrolyte conditions, excited-state proton transfer from photoacids to solution can be kinetically inhibited,[59] thus attenuating photogeneration of mobile H^+, as supported by the data in **Figure 2e**. Therefore, photoacids most likely to perform excited-state proton transfer are probably located at the membrane|solution interfaces where a gradient in pH exists across the space–charge region, and which is also the optimal location for efficient charge separation of photogenerated mobile charged species in traditional electronic semiconductor solar cells. This, coupled with the observation of an illumination-direction-independent *sign* and *magnitude* of V_{oc}, suggests that photogenerated majority-carrier H^+ are collected over the thickness of HPTSA-modified PFSA (50.8 μm) and/or that photo-induced local polarizations generate differences in electric potential that are sensed at the Ag/AgCl wires and are independent on the direction of illumination.

The hypothesis of a tens-of-microns collection length seems unlikely based on the reasonable upper limit for the diffusion coefficient of H^+ in Nafion (9.31 x 10^{-5} cm^2/s in bulk water)[42] and an effective time constant for the photoacid dye sensitization Förster cycle, which is gated by the ~5 ns excited-state lifetime of the photoacid in strongly acidic conditions like those in Nafion, because this suggests a diffusion length of ~7 nm. This diffusion length is the average transport distance for a photogenerated H^+ prior to recombination with a deprotonated photoacid; although, the diffusion length prior to recombination with $OH^-(aq)$ is considerably larger. Under our experimental conditions on average there are only 10^{-14} M OH^-, which is the same as 30,592 OH^- molecules per cm^2 of 50.8 μm thick membrane. Presuming that photogenerated H^+ sample positions within a hemisphere of 50.8 μm radius during transport across the 50.8 μm thick

membrane, the average number of OH^- encounters experienced by each photogenerated H^+ before reaching the other membrane|solution interface is $1 - 2$, as calculated in the Supplementary Information in the subsection titled "Average Number of OH^- Encounters by a Photogenerated H^+ in Protonated Nafion." Such a majority-carrier device could conceivably collect charges stochastically over such large distances,[69] but only in the absence of deprotonated photoacids, because they limit this transport distance to ~7 nm.

Given that deprotonated photoacids will be present under illumination, we hypothesize that photo-induced local polarizations are responsible for the observation of "reverse" photovoltaic action by a process that we term electrolyte-crossover-induced bulk membrane polarization (ECIBMP). For ECIBMP, we propose that photogenerated-H^+/deprotonated-HPTSA pairs, and not mobile charged species pairs that are commonly generated in traditional electronic solar cells, form collectively *asymmetric* space–charge regions in the *bulk* of HPTSA-modified PFSA (Figure 3, in green). In order to observe a non-zero value for V_{oc} a net asymmetry is required. The observation of "reverse" photovoltaic action is consistent with the driving force for charge separation being liquid-junction potentials that form due to diffusion of HCl toward the rectifying junction in the dark. This hypothesis is also consistent with the fact that the magnitude of measured V_{oc} values are directly related to presumed magnitudes of ϕ_{LJ}^{mem} values (**Table 2**). Moreover, such a bulk phenomenon would result in an illumination-direction-independent *sign* and *magnitude* of V_{oc}, as we observed.

Mechanistically, we envision that during the lifetime of photogenerated H^+, H^+ diffuse away from ground-state deprotonated HPTSA and toward the rectifying junction. However, photogenerated H^+ also experience Coulombic attraction to anionic ground-state deprotonated HPTSA via processes that are similar to those that occur in formation of liquid-junction potentials

in a solution and Dember potentials due to ambipolar diffusion in electronic semiconductors.[70]

Therefore, H⁺ resides on average at a distance equal to the Debye/Bjerrum length for the two ions

(**Figure 7**), which is on the order of 1 nm per

HPTSA at the approximate concentration of

HPTSA present in **DSM-H**. (The concentration of

HPTSA was approximated to be 77 mM using the

Beer–Lambert law and the molar absorptivity of

HPTSA(aq) at 405 nm, a pathlength equal to the

thickness of Nafion NR-212 (50.8 µm), and the

optical density of **DSM-H** at 405 nm, which was

Figure 7. Scheme depicting the proposed mechanism for "reverse" photovoltaic action, ECIBMP, in ionic membrane–liquid assemblies. A gradient in HCl across the membrane drives dipole formation between photogenerated H⁺ and various counterion species.

approximated to be ten times larger than that measured for **DSM-L** (0.664) because the synthetic

protocol used a ten times more dilute dye solution.) This dipolar state generated by a single charge

pair exhibits a small electric field in comparison to projected electric field strengths at space–

charge regions near the membrane|solution interface, which are up to ~240 mV and drop over

several nanometers. Excitonic electrostatically bound charges will separate at these space–charge

regions to generate mobile charged species and will result in typical photovoltaic action, but the

number of species photogenerated near those interfacial regions (over <10 nm) is likely so small

compared to those generated in the membrane bulk (over 50.8 µm) that any effects from excitonic

charge-separation events are likely undetectable given the sensitivity of our measurement

capabilities. Regeneration of ground-state deprotonated HPTSA by a nearby H⁺ results in

formation of no net chemical species, however we suspect that spatial distributions of H⁺ under

illumination differ from those in the dark, where most H⁺ are electrostatically attracted to sulfonate

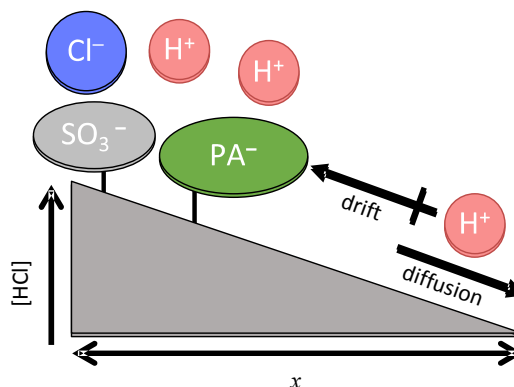groups covalently anchored to the polymer, or less commonly, mobile Cl⁻. In either case, on

average electric potential differences formed by ECIBMP will increase the magnitude of ϕ_{LJ}^{mem}

values present in the dark due to similar ion-crossover phenomena.

While reported V_{oc} values are likely indicative of the properties of HPTSA-modified PFSA,

as mentioned above, photocurrent values are not, due to the low ionic strength and large transport

distances of ions in the aqueous electrolytes between the membrane and each Ag/AgCl wire in

comparison to solely across the membrane. However, an upper limit to the local current density

across only HPTSA-modified PFSA can be approximated by assuming a unity quantum yield for

conversion of absorbed photons to ionic current and assuming a membrane conductivity of ~50

mS/cm, which is the approximate value reported for commercial Nafion at room temperature when

fully hydrated and protonated using H_2SO_4(aq).[71,72] A relation between observed V_{oc} values and

ideal short-circuit photocurrent values can be obtained using Ohm's law,

$$E = iR = jASR = j/ASC = j\ell/\sigma \tag{14}$$

where i is the current (A), R is the resistance (Ω), j is the current density (A/cm^2), ASR is the area-

specific resistance (Ω-cm^2), ASC is the area-specific conductance (S/cm^2), ℓ is the thickness of the

membrane (cm), and σ is the conductivity of the membrane (S/cm). Solving this formula for the

current density as a function of the potential and adding a constant ideal photocurrent in the

absence of other losses, $j_{ph,ideal}$, one obtains the following,

$$j = \sigma E/\ell - j_{ph\text{-}sc,ideal} \tag{15}$$

Under open-circuit conditions, $j = 0$ and thus $j_{ph,ideal} = \sigma V_{oc}/\ell$. Using the maximum measured $V_{oc} \approx$

4 mV, which seems to saturate at high light intensities and requires an irradiance of $> \sim$100

mW/cm^2, one calculates that $j_{ph,ideal} \approx$ (5 x 10^{-2} S/cm) (4 x 10^{-3} V) / (5 x 10^{-3} cm) = 40 mA/cm^2. It

is remarkable that this value is within error of the value predicted by assuming that every incident

photon is converted into current as a mobile H^+. Further refinement of this analysis would lead to a smaller value for $j_{ph,ideal}$, because the conductivity used for this calculation is likely overestimated given that it was measured in the absence of interfacial space–charge regions. But this effect is offset by the fact that every absorbed photon does not generate a mobile H^+, as evidenced by photoluminescence data (**Figure 2e and S14**), which suggest that ~10% of photoacids in **DSM-H1** undergo the Förster cycle. Collectively, however, this simple Ohm's law analysis does suggest that it is reasonable to assume that photogenerated H^+ are capable of generating a photocurrent. Using this above information one can approximate the average concentration of photogenerated H^+, by dividing $j_{ph,ideal}$ by the membrane thickness (5.08×10^{-3} cm) and the Faraday constant, and multiplying it by the time it takes to regenerate the deprotonated photoacid, which in aqueous 1 M acidic solutions is limited by the excited-state lifetime to ~5 ns. This results in a projected steady-state increase in the concentration of H^+ of ~4×10^{-10} M, which is intermediate in concentration between that of Cl^- coions and OH^- in the dark.

Outlook for use of photoacid-modified ion-exchange membranes for light-driven desalination. Minimum voltages required to drive desalination are not very large, thermodynamically requiring at most ~50 – 200 mV depending on the salinity of the water source, e.g. seawater or brackish, and desired output salinity, e.g. potable or for agriculture, and before considering overpotential losses. With further increase in performance, illumination of HPTSA-modified PFSA could be used to *indirectly* drive desalination of salt water via intermediate electricity. However, a benefit of using an ion-exchange membrane is that it could be contacted directly by aqueous salt solutions on each side to *directly* drive desalination. This requires that Donnan space–charge regions are generated from equilibration of majority-carrier salt cations, such as Na^+ or K^+, with minority-carrier

excluded salt anions, such as Cl^-, which we have demonstrated is possible.[73] In this configuration, however, photovoltages must be of the traditional sign so that photogenerated cationic charged species transport toward and across the low-impedance charge-collection junction, which is the side of the membrane that contacts the solution containing the larger salt concentration. Preliminary data obtained from **DSM-H1** using pKCl 1‖3 suggest that in this configuration "reverse" photovoltaic action is still observed (**Figure S14**).

Further requirements to enable dye-sensitized membrane–liquid-junction constructs to *directly* drive desalination likely include that photoacid and/or photobase dye sensitizers be replaced with photo-ionophores, which change binding strength to a cation or anion upon photoexcitation. Such molecules have been reported previously,[74] but have not been optimized for this application. Moreover, a single homogeneous ion-exchange membrane directly wetted by salt solutions on each side will not be able to drive the desired ion-pumping chemistry. This is because in the absence of a low-impedance junction between the ion-exchange membrane and the concentrated electrolyte, e.g. like a so-called tunnel junction, net chemical reactions cannot be driven by light that require more free energy than the reactions used to set the built-in potentials of the rectifying charge-separation junction and low-impedance charge-collection junction. This does not limit photovoltaic devices, where light does not generate any net chemical species and therefore the entire photovoltage can be used to perform useful work. However, in devices that drive net chemistry, such as solar fuels constructs, chemical reactions of interest, such as H_2 evolution and O_2 evolution, cannot be used to dictate the built-in potential of both the rectifying and low-impedance junction on each side of a homogeneously-doped electronic semiconductor, because photovoltages due to solar irradiation of terrestrial constructs will not exceed the free energy difference of these reactions, e.g. 1.23 V. This challenge existed in our previous buried-

junction bipolar-membrane designs,[14,15] where contacting phases consisted of aqueous acid and aqueous base, which determined built-in potentials but limited photovoltages to values that were incapable of driving net generation of acid, as H^+(aq) and a solvated counterion, and base, as OH^- (aq) and a solvated counterion.[75] Therefore, analogous to design principles in semiconductor–liquid junctions, low-impedance junctions are typically formed using an intervening contact that decouples the selectivity of transport from the thermodynamics of the contacting phase. In this regard, a highly doped membrane could be used to form a solid-state low-impedance junction to a dye-sensitized membrane–liquid-junction construct prior to contacting the concentrated electrolyte chamber.[35]

Dye-sensitized membrane–liquid-junction constructs will also suffer from challenges that are common for ion-exchange membranes in desalination technologies, such as biofouling, scaling, instability, etc.[76,77] However, if these obstacles can be overcome, dye-sensitized membrane–liquid-junction constructs afford a flexible platform for desalination that can be used as an alternative to existing technologies (reverse osmosis, solar-thermal desalination, electrodialysis, etc.) by enabling a small-footprint autonomous desalination device.[34] The proposed technology would be most beneficial for use in remote desalination of brackish water, where reverse osmosis is not cost competitive,[35] and transporting water is too expensive.[78] For example, salinity requirements for agriculture are often less strict compared to requirements for potable water, offering an avenue for feed water partially contaminated with saline to be passively desalinated for use in irrigation, and reused via collection of runoff. Collectively, our work provides guidance for the community to help advance these device designs with hopes of ultimately realizing a small-footprint autonomous device for distributed clean water generation.

Conclusions

Traditional perfluorosulfonic acid ion-exchange membranes were covalently modified with custom photoacid dye molecules and wetted by an aqueous acidic electrolyte on each side. Using a custom electrochemical cell and Ag/AgCl wires as potential-sensing electrodes, membrane potentials were accurately quantified in the dark and under $0.5 - 6.5$ Suns equivalent excitation. In the dark, measured net electric potential differences were similar to those expected from Donnan theory, while in the light, open-circuit photovoltages were largest in magnitude when the difference in interfacial Donnan electric potentials between the rectifying charge-separation junction and the low-impedance charge-collection junction were largest. Maximum open-circuit photovoltages of ~4 mV were measured albeit their sign was opposite ("reverse") of that expected based on the sign of net electric potential differences across the membrane. Dye sensitizers consisting of photoacids that could perform excited-state proton transfer were more effective at exhibiting photovoltaic action than negative control dyes that could not. However, mechanistic details gleaned from nanosecond transient absorption spectroscopy suggest that even state-of-the-art photoacids only photogenerate mobile protons, which in part limits performance because protons are majority-carrier mobile charged species. We hypothesize that the observation of "reverse" photovoltaic action is due to electrolyte-crossover-assisted charge separation that results in bulk membrane polarization, which are the liquid-junction analogs of Dember potentials in electronic semiconductors. Our results further the basic understanding of means by which light can be used exhibit photovoltaic action through transport and reactivity of ions. These results also guide next research steps, which include the development of photoacids and/or photobases that exhibit a larger change in acidity upon photoexcitation, such that both majority-carrier and minority-carrier species are photogenerated. Moreover, to realize light-driven ion pumps for

application in direct desalination of salt water, critical needs include the development of photo-ionophores, to directly photogenerate non-protonic ions, and highly doped membranes, to form low-impedance junctions between low-doped ion-exchange membranes and concentrated electrolytes.

Author Contributions

S.L. contributed to the design of experiments, prepared *all* samples and performed *all* measurements including subsequent analysis and interpretation of *all* data reported in this manuscript, and contributed to preparation of the manuscript. W.W. and J.C. contributed to the design of initial experiments, prepared initial samples and performed initial electrochemical and transient absorption measurements including subsequent data analysis and interpretation. J.C. and S.L. also constructed our custom nanosecond transient absorption and time-resolved photoluminescence spectroscopy system. S.A. proposed the research and contributed to experimental design, data interpretation, and preparation of the manuscript.

Acknowledgements

Competing Interests

Co-authors are co-inventors on the following pending patent applications that are relevant to this article: US20180065095 and WO2018049061 (S.A., W.W., and J.M.C.), US20190217255 and WO2019191326 (S.A., J.M.C., and W.W.). S.A. received sponsored research funding support by Nissan Chemical Corporation for work related to that reported in this article.

References

1   K. Lehovec, *Zeitschrift fur Naturforsch. - Sect. A J. Phys. Sci.*, 1946, **1**, 258–263.

2   K. Lehovec, *Opt.*, 1946, **1**, 268.

3   K. Lehovec, *Phys. Rev.*, 1948, **74**, 463–471.

4   P. Würfel and U. Würfel, *Physics of solar cells: From basic principles to advanced concepts, second updated and expanded edition*, Wiley-VCH, 3rd edn., 2009.

5   U. Würfel, A. Cuevas and P. Würfel, *IEEE J. Photovoltaics*, 2015, **5**, 461–469.

6   W. Shockley, *Bell Syst. Tech. J.*, 1949, **28**, 435–489.

7   S. Ardo and G. J. Meyer, *Chem. Soc. Rev.*, 2009, **38**, 115–164.

8   B. O'Regan and M. Grätzel, *Nature*, 1991, **353**, 737–740.

9   A. Hagfeldt, G. Boschloo, L. Sun, L. Kloo and H. Pettersson, *Chem. Rev.*, 2010, **110**, 6595–6663.

10   M. K. Brennaman, R. J. Dillon, L. Alibabaei, M. K. Gish, C. J. Dares, D. L. Ashford, R. L. House, G. J. Meyer, J. M. Papanikolas and T. J. Meyer, *J. Am. Chem. Soc.*, 2016, **138**, 13085–13102.

11   W. Cao and J. Xue, *Energy Environ. Sci.*, 2014, **7**, 2123–2144.

12   O. Inganäs, *Adv. Mater.*, 2018, **30**, 1800388.

13   W. White, C. D. Sanborn, R. S. Reiter, D. M. Fabian and S. Ardo, *J. Am. Chem. Soc.*, 2017, **139**, 11726–11733.

14   W. White, C. D. Sanborn, D. M. Fabian and S. Ardo, *Joule*, 2018, **2**, 94–109.

15   W. White, S. Luo, R. Bhide, C. D. Sanborn, M. S. Baranov, K. M. Solntsev and S. Ardo, in *Physical Chemistry of Semiconductor Materials and Interfaces XVIII*, SPIE, 2019, vol. 11084, p. 12.

16   L. M. Tolbert and K. M. Solntsev, *Acc. Chem. Res.*, 2002, **35**, 19–27.

17   S. J. Fonash, *Solar Cell Device Physics*, Academic Press, Burlington, 2nd edn., 2010.

18   M. X. Tan, P. E. Laibinis, S. T. Nguyen, J. M. Kesselman, C. E. Stanton and N. S. Lewis,

in *Progress in Inorganic Chemistry*, Wiley, 2007, vol. 41, pp. 21–144.

19   M. G. Walter, E. L. Warren, J. R. McKone, S. W. Boettcher, Q. Mi, E. A. Santori and N. S. Lewis, *Chem. Rev.*, 2010, **110**, 6446–6473.

20   A. C. Nielander, M. R. Shaner, K. M. Papadantonakis, S. A. Francis and N. S. Lewis, *Energy Environ. Sci.*, 2015, **8**, 16–25.

21   N. S. Lewis, *J. Electrochem. Soc.*, 1984, **131**, 2496.

22   R. L. Grimm, M. J. Bierman, L. E. O'Leary, N. C. Strandwitz, B. S. Brunschwig and N. S. Lewis, *J. Phys. Chem. C*, 2012, **116**, 23569–23576.

23   A. Bansal and N. S. Lewis, *J. Phys. Chem. B*, 1998, **102**, 4058–4060.

24   R. E. Kalan, M. A. Russell, J. L. Taylor and R. L. Grimm, *J. Electrochem. Soc.*, 2017, **164**, H798–H804.

25   M. A. Russell, R. E. Kalan, A. J. Pugliese, A. D. Carl, C. P. Masucci, N. C. Strandwitz and R. L. Grimm, *J. Electrochem. Soc.*, 2019, **166**, H608–H614.

26   J. Newman and K. E. Thomas-Alyea, *Electrochemical Systems*, 3rd edn., 2004.

27   J. O. Bockris and A. K. N. Reddy, *Modern Electrochemistry 1: Ionics*, Springer US, 2nd edn., 1998.

28   P. Henderson, *Zeitschrift für Phys. Chemie*, 1907, **59**, 118.

29   D. E. Goldman, *J. Gen. Physiol.*, 1943, **27**, 37–60.

30   K. R. Ward, E. J. F. Dickinson and R. G. Compton, *J. Phys. Chem. B*, 2010, **114**, 10763–10773.

31   R. S. Reiter, W. White and S. Ardo, *J. Electrochem. Soc.*, 2016, **163**, H3132–H3134.

32   F. G. Donnan, *Chem. Rev.*, 1924, **1**, 73–90.

33   G. S. Manning, *J. Chem. Phys.*, 1969, **51**, 924–933.

34   S. Ardo, W. White, C. D. Sanborn, J. M. Cardon, R. S. Reiter and E. Schwartz, *Light-driven ion-pumping membrane systems.*, US20180065095 A1, USA, 2018.

35   S. Ardo, E. Schwartz, J. Liu, J. M. Cardon, W. White, K. Tkacz, L. A. Renna, M. A. Modestino, D. Blanco, L. Schulte and R. Bhide, *Systems and methods for integrated solar photodialysis*, US20190217255 A1, USA, 2019.

36   C. D. Sanborn, J. V. Chacko, M. Digman and S. Ardo, *Chem*, 2019, **5**, 1648–1670.

37   Reference Air Mass 1.5 Spectra | Grid Modernization | NREL, https://www.nrel.gov/grid/solar-resource/spectra-am1.5.html, (accessed 31 January 2021).

38   H. Y. Chen and S. Ardo, *Nat. Chem.*, 2018, **10**, 17–23.

39   A. Kusoglu and A. Z. Weber, *Chem. Rev.*, 2017, **117**, 987–1104.

40   The Chemours Company, *Nafion NR211 and NR212 Ion Exchange Materials*, 2017.

41   J. Kamcev, D. R. Paul and B. D. Freeman, *J. Mater. Chem. A*, 2017, **5**, 4638–4650.

42   A. J. Bard and L. R. Faulkner, *Electrochemical Methods Fundamentals and Applications, Second Edition*, Wiley, Second., 2001.

43   S. Hu, M. Lozada-Hidalgo, F. C. Wang, A. Mishchenko, F. Schedin, R. R. Nair, E. W. Hill, D. W. Boukhvalov, M. I. Katsnelson, R. A. W. Dryfe, I. V. Grigorieva, H. A. Wu and A. K. Geim, *Nature*, 2014, **516**, 227–230.

44   J. L. Achtyl, R. R. Unocic, L. Xu, Y. Cai, M. Raju, W. Zhang, R. L. Sacci, I. V. Vlassiouk, P. F. Fulvio, P. Ganesh, D. J. Wesolowski, S. Dai, A. C. T. Van Duin, M. Neurock and F. M. Geiger, *Nat. Commun.*, 2015, **6**, 1–7.

45   G. J. Moody, R. B. Oke and J. D. R. Thomas, *Analyst*, 1969, **94**, 803–804.

46   T. Kim, B. E. Logan and C. A. Gorski, *Energy Environ. Sci.*, 2017, **10**, 1003–1012.

47   S. W. Boettcher, S. Z. Oener, M. C. Lonergan, Y. Surendranath, S. Ardo, C. Brozek and P. A. Kempler, *ACS Energy Lett.*, 2021, **6**, 261–266.

48   J. Tauc and M. Závětová, *Czechoslov. J. Phys.*, 1959, **9**, 572–577.

49   W. E. Moerner, in *Encyclopedia of Materials: Science and Technology*, Elsevier, 2001, pp. 6961–6968.

50   L. Ju, J. Velasco, E. Huang, S. Kahn, C. Nosiglia, H. Z. Tsai, W. Yang, T. Taniguchi, K. Watanabe, Y. Zhang, G. Zhang, M. Crommie, A. Zettl and F. Wang, *Nat. Nanotechnol.*, 2014, **9**, 348–352.

51   F. E. Osterloh, M. A. Holmes, J. Zhao, L. Chang, S. Kawula, J. D. Roehling and A. J. Moulé, *J. Phys. Chem. C*, 2014, **118**, 14723–14731.

52   A. Pockett, D. Raptis, S. M. P. Meroni, J. Baker, T. Watson and M. Carnie, *J. Phys. Chem. C*, 2019, **123**, 11414–11421.

53   T. Deppe and J. N. Munday, *ACS Photonics*, 2020, **7**, 1–9.

54   L. Schulte, W. White, L. A. Renna and S. Ardo, *Joule*, accepted.

55   G. M. Su, W. White, L. A. Renna, J. Feng, S. Ardo and C. Wang, *ACS Macro. Lett.*, 2019,

8, 1353–1359.

56   G. Giro, P. G. Di Marco and G. Casalbore, *Inorganica Chim. Acta*, 1981, **50**, 201–204.

57   A. B. Kotlyar, N. Borovok, S. Raviv, L. Zimanyi and M. Gutman, *Photochem. Photobiol.*, 1996, **63**, 448–454.

58   G. Phun, et al., *Energy Environ. Sci.*, to be submitted shortly.

59   J. R. Lakowicz, in *Principles of Fluorescence Spectroscopy*, Springer, 3rd edn., 2006, pp. 260–262.

60   T.-H. Tran-Thi, T. Gustavsson, C. Prayer, S. Pommeret and J. T. Hynes, *Chem. Phys. Lett.*, 2000, **329**, 421–430.

61   E. Pines and D. Huppert, *Chem. Phys. Lett.*, 1986, **126**, 88–91.

62   R. T. Ross and T. L. Hsiao, *J. Appl. Phys.*, 1977, **48**, 4783–4785.

63   M. Eigen, *Pure Appl. Chem.*, 1963, **6**, 97–116.

64   T. Förster and S. Völker, *Chem. Phys. Lett.*, 1975, **34**, 1–6.

65   C. L. Perrin, T. J. Dwyer and P. Baine, *J. Am. Chem. Soc.*, 1994, **116**, 4044–4049.

66   H. L. Xia, S. Ardo, A. A. N. Sarjeant, S. Huang and G. J. Meyer, *Langmuir*, 2009, **25**, 13641–13652.

67   M. Eigen, *Angew. Chemie Int. Ed. English*, 1964, **3**, 1–19.

68   R. Bhide, et al., *Nat. Chem.*, to be submitted shortly.

69   G. Hodes and P. V. Kamat, *J. Phys. Chem. Lett.*, 2015, **6**, 4090–4092.

70   S. J. Fonash and S. Ashok, *Appl. Phys. Lett.*, 1979, **35**, 535–537.

71   T. A. Zawodzinski, *J. Electrochem. Soc.*, 1993, **140**, 1041.

72   S. Shi, T. J. Dursch, C. Blake, R. Mukundan, R. L. Borup, A. Z. Weber and A. Kusoglu, *J. Polym. Sci. Part B Polym. Phys.*, 2016, **54**, 570–581.

73   W. Gaieck, et al., *J. Chem. Educ.*, to be submitted shortly.

74   M. D. Turlington, L. Troian-Gautier, R. N. Sampaio, E. E. Beauvilliers and G. J. Meyer, *Inorg. Chem.*, 2018, **57**, 5624–5631.

75   W. Shockley and H. J. Queisser, *J. Appl. Phys.*, 1961, **32**, 510–519.

76   M. Elimelech and W. A. Phillip, *Science (80-.).*, 2011, **333**, 712–717.

77   S. K. Patel, C. L. Ritt, A. Deshmukh, Z. Wang, M. Qin, R. Epsztein and M. Elimelech, *Energy Environ. Sci.*, 2020, **13**, 1694–1710.

78   Y. Zhou and R. S. J. Tol, *Water Resour. Res.*, 2005, **41**, 1–10.